Drainage rearrangement in an intra-continental mountain belt: A case study from the central South Tian Shan, Kyrgyzstan

Lingxiao Gong[1], Peter van der Beek[1], Taylor F. Schildgen[1,2], Edward R. Sobel[1], Simone Racano[1], Apolline Mariotti[2]

[1]Institut für Geowissenschaften, Universität Potsdam, Potsdam, 14476, Germany
[2]GFZ German Research Centre for Geosciences, Potsdam, 14473, Germany

Correspondence to: Lingxiao Gong (gong@uni-potsdam.de)

Abstract

Fluvial drainage patterns in orogenic belts reflect the interaction between tectonics, climate, and lithology. The central South Tian Shan displays a complex fluvial drainage pattern that shifts from longitudinal (flowing parallel to mountain ranges) in the west to transverse (flowing across ranges) in the east. Whether such drainage patterns reflect underlying patterns of tectonic deformation, lithology, climatic changes, or the influence of surface processes within a drainage basin is often unclear. We focus here on the anomalously large Saryjaz catchment of SE Kyrgyzstan, which marks the transition between longitudinal and transverse drainage. We analyse topographic and fluvial metrics including slope, river steepness (k_{sn}) and the integral proxy χ along the river profile, and map the spatial distribution and characteristics of knickpoints to discern the possible controls on the observed drainage pattern. We discriminate between knickpoints of different origin: tectonic, lithologic, glacial, and those linked to transient waves of incision. We find a series of transient knickpoints in tributaries downstream of a sharp 180° bend in the main stem of the Saryjaz River, which also marks a striking increase in channel steepness. Both observations indicate accelerated incision along this lower reach of the catchment. Knickpoint elevations decrease downstream, whereas incision depth, χ values of knickpoints (measured from the tributary junctions) and k_{sn} values and ratios are constant among tributaries. These results suggest that incision is driven "top-down" by a large-magnitude river-capture event rather than "bottom-up" by base-level fall. We estimate an erodibility parameter from [10]Be derived catchment-average denudation rates and use this to estimate the celerity of knickpoints. We find that the knickpoints started retreating at a similar time, between ca. 1.5 and 4.4 Myr ago. Considering the river patterns and the timing constraints, we suggest that this capture event was likely driven by the overfill of Neogene intermontane basins, potentially affected by both tectonic and climate factors.

1 Introduction

Map patterns of rivers result from the interaction between climate, tectonics and lithology (Hovius, 1996; Whipple, 2004; Babault et al., 2012; Seagren and Schoenbohm, 2019; Seagren et al., 2022; Wolf et al., 2022). River patterns in turn play a key role in source-to-sink relationships (Gupta, 1997; Horton and Decelles, 2001), biodiversity(Craw et al., 2016; Boschman et al., 2023; Stokes et al., 2023), and tectonic evolution (e.g. Garcia-Castellanos and Jiménez-Munt, 2015; Jourdon et al., 2018;

Viaplana-Muzas et al., 2019). The occurrence of both longitudinal (i.e., strike-parallel) and transverse (i.e., strike-perpendicular) drainage patterns has long been observed and discussed in different tectonic settings, from collisional (e.g., Himalaya) to intra-continental (e.g., High Atlas, Pyrenees) or accretionary (e.g., Andes), associated with either thin- or thick-skinned deformation mechanisms (e.g. Gupta, 1997; Babault et al., 2012; Seagren et al., 2022). One common drainage-

35 evolution model considers that longitudinal drainage patterns are controlled by active structures (e.g. faults and folds). Growth of the mountain belt steepens regional and local slopes, thereby favouring the development of transverse drainage patterns that flow parallel to the regional slopes to replace the relatively low-energy longitudinal drainage (Babault et al., 2012; Struth et al., 2015). Another model, applied in particular to the broken Andean foreland of NW Argentina, suggests a stable and long-lived longitudinal drainage network developing from an initial transverse pattern, likely controlled by the inconsistent regional

40 taper and locally high relief (Seagren et al., 2022). Conversely, Wolf et al. (2022) did not describe evolutionary stages of drainage systems, but rather emphasized that longitudinal or transverse drainage networks can reflect steady-state forms of tectonically or erosionally dominated mountain belts, respectively.

As the biggest intracontinental orogen in Central Asia, the Tian Shan provides a natural laboratory to study the complex relationships among Cenozoic deformation, topography, glacial erosion, and drainage response. GPS data show that modern

45 N-S shortening rates across the Tian Shan decrease eastward from ~17.5 mm/yr to ~3 mm/yr, indicating strong spatial differences in recent deformation rates (Fig. 1a; Abdrakhmatov et al., 1996; Wang et al., 2001; Yang et al., 2008). Topographic growth within the Tian Shan and Pamir likely started between 12 and 7 Ma, and appears to continue today, as tectonic uplift has been shown to outpace modern erosional denudation in the eastern Tian Shan (Charreau et al., 2017, 2023; Li et al., 2022; Richter et al., 2022). The onset of Plio-Pleistocene glaciations, possibly starting from around 3 to 2.5 Myr ago (Ma) based on

50 records of increased erosional variability (Charreau et al., 2011; Puchol et al., 2017), likely affected relief development, and may have triggered the reactivation of tectonic structures (Sobel et al., 2006b). Within this tectonic and climatic context, the South Tian Shan exhibits a significant contrast between a longitudinal drainage pattern in the west and transverse drainage in the east (Fig. 1). However, it is not clear how or if the drainage pattern responded to Cenozoic structural reactivation and the uplift of individual ranges, a major change in climate, or the impacts of locally intense glacial erosion.

55 To unravel these complexities, we investigated the transition area between the regions of longitudinal and transverse drainage: the anomalously large Saryjaz catchment, which drains the highest part of the South Tian Shan, and includes two Neogene intermontane basins: the Ak Shyyrak and Saryjaz basins (Figs. 1, 2). We combine quantitative analysis of topography using fluvial metrics (i.e. slopes, channel steepness, integral proxy χ), with mapping and characterization of knickpoints throughout the catchment. Based on multiple lines of evidence that point to a landscape undergoing a transient adjustment (e.g. prominent

60 migrating knickpoints, systematic shifts in channel steepness values), we next consider whether tectonic forcing or drainage capture can explain the observations. We use recently published denudation rates inferred from ^{10}Be concentrations of river sands to estimate an erodibility parameter and place constraints on the timing of drainage evolution. While this type of analysis is common in tectonically active regions, only a few studies have considered how geomorphic metrics may be used to detect drainage-capture events (Yanites et al., 2013; Giachetta and Willett, 2018; Penserini et al., 2023; Rohrmann et al., 2023). Our

65 estimates for the onset of the transient adjustment furthermore help to determine the role of regional forcing conditions on the drainage evolution.
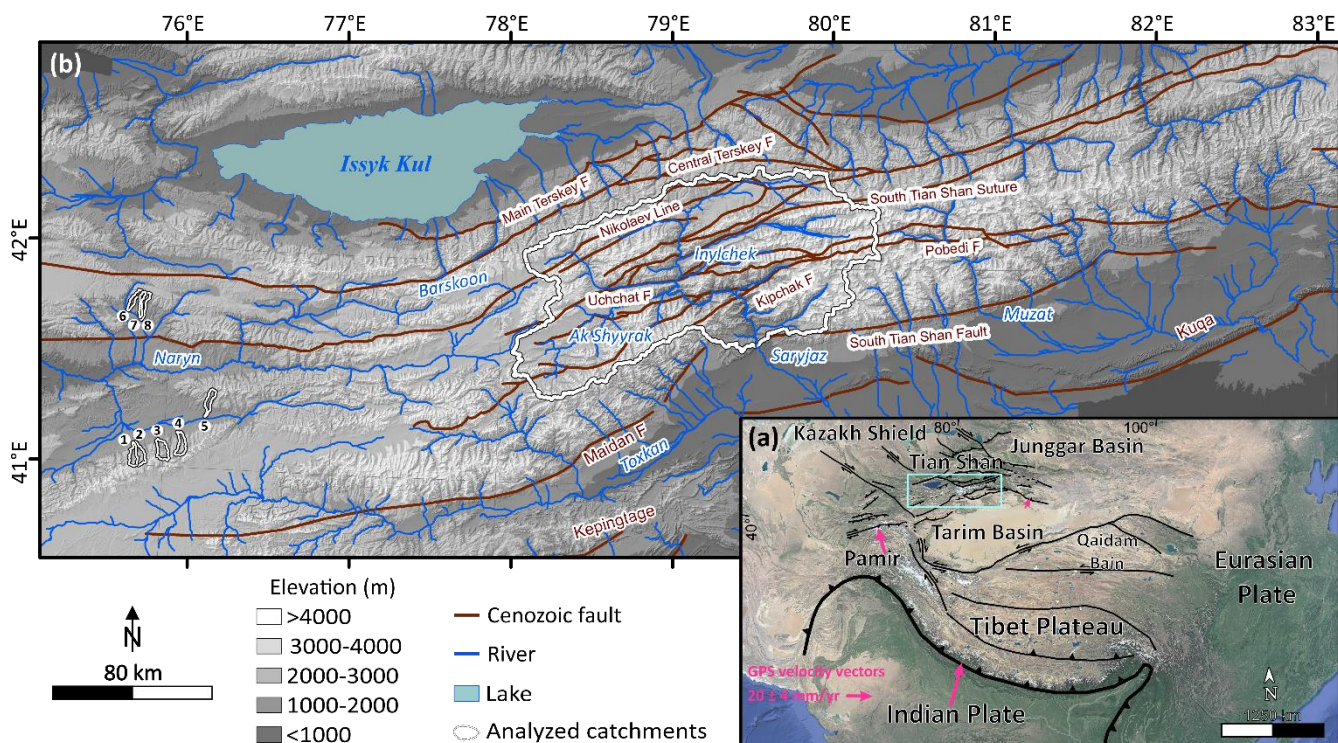
Figure 1 (a) Overview of the Tian Shan, including major fault structures and present shortening rates from GPS velocity vectors (mm/yr) (Wang et al., 2001; Yang et al., 2008; basemap from © Google Earth); (b) Shaded topography map of the central South Tian Shan showing main Cenozoic faults and rivers, edited after Mikolaichuk et al. (2008). The Saryjaz catchment is outlined, as are the
70 **small catchments used for cosmogenic erosion-rate determinations (labelled 1 to 8 on the left side of the map).**

2 Background

2.1 Topographic and climatic setting

The South Tian Shan is a W-E trending mountain belt, characterized by a high-elevation, high-relief landscape, with numerous peaks rising to > 4000 m above sea level (Fig. 1). Piedmont elevations to the north of the mountain belt, in the intermontane
75 Issyk-Kul basin and adjacent Zhaosu–Tekesi Depression, are around 1500-2000 m. The Tarim Basin acts as a foreland basin flanking the South Tian Shan, lying at elevations between 800 and 1000 m. Between the Tarim Basin and the Tian Shan, the Kepingtage and Kuqa ranges reach elevations of ~ 3000 m (Fig. 1b). The South Tian Shan is characterized by transient landscapes, as documented by a widespread high-standing relict Mesozoic low-relief surface and elevated intermontane basins (Abdrakhmatov et al., 2001; Morin et al., 2019).
80 Within the South Tian Shan, elevations, together with relief and slopes, decrease to the east and west from a central core at about 80 ºE latitude. Two major peaks, Khan Tengri (7010 m) and Jengish Chokusu (or Pobeda; 7439 m), rise in this core of

the orogen, at the boundary between Kyrgyzstan, Kazakhstan and China (Fig. 2). In contrast, the width of the mountain belt decreases from west to east, forming an elongated triangle shape. Drainage basins in the east are mostly characterized by transverse streams, whereas to the west, they show longitudinal patterns. The transition zone between these two drainage

85   patterns hosts both the highest topography and the Saryjaz River catchment (Figs. 1, 2). The geometry of the Saryjaz River shows a combination of longitudinal and transverse components: the upstream reaches, originating in the Khan Tengri and Jengish Chokusu ranges, flow to the southwest, parallel to the mountains and valleys, before gradually turning to the south with several sharp bends, including a prominent "U-turn" near the eastern limit of the Ak Shyyrak Basin (Fig. 2b-c). Several east-flowing longitudinal tributaries also form part of this upstream part of the catchment. Downstream of the "U-turn", the

90   main stem of the river flows to the SE, cutting transversely through the mountain range and into the Tarim Basin (Fig. 1, 2).
The late-Cenozoic climate of central Asia is marked by a continuous cooling trend since ca. 15 Ma, with particularly strong cooling during the Plio-Pleistocene global glaciations (Zachos et al., 2001; Macaulay et al., 2016; Frisch et al., 2019; Richter et al., 2022). Global cooling, together with topographic growth of the Pamir and Tian Shan, largely contributed to the aridification of the Tarim Basin and its surroundings (Sun et al., 2017; Richter et al., 2022). Average precipitation throughout

95   the Tian Shan currently ranges between ~ 200 and 300 mm, varying from 455 mm in the western Tian Shan to only 97 mm in the east (Chen et al., 2016; Guan et al., 2022).
Glaciers have played an important role in the late-Cenozoic topographic and drainage evolution of the Tian Shan. The South Tian Shan shows widespread glacial landforms, especially in regions with elevations over 3000 to 3500 m (Stroeven et al., 2013). The geomorphologically recorded maximum positions of glaciers in the Inylchek and Saryjaz valleys occurred during

100   the Last Glacial Maximum (MIS 2), based on ^{10}Be exposure dating of moraine sequences, and corresponds to an estimated equilibrium-line-altitude (ELA) depression of 225 m (Lifton et al., 2014). Former glacial extents, and glacial imprints on the landscape, are generally more extensive on the north flank of the South Tian Shan than on its south flank. This difference has been argued to control differential piedmont river incision, which is significantly higher on the northern than on the southern piedmont of the South Tian Shan (Malatesta and Avouac, 2018). However, the Saryjaz catchment, draining to the southern

105   piedmont of the Tian Shan, is an exception, as it was extensively glaciated but has not incised its piedmont significantly. Malatesta and Avouac (2018) explained this anomaly as a result of ongoing evacuation of sediment from the upstream glacial valleys.
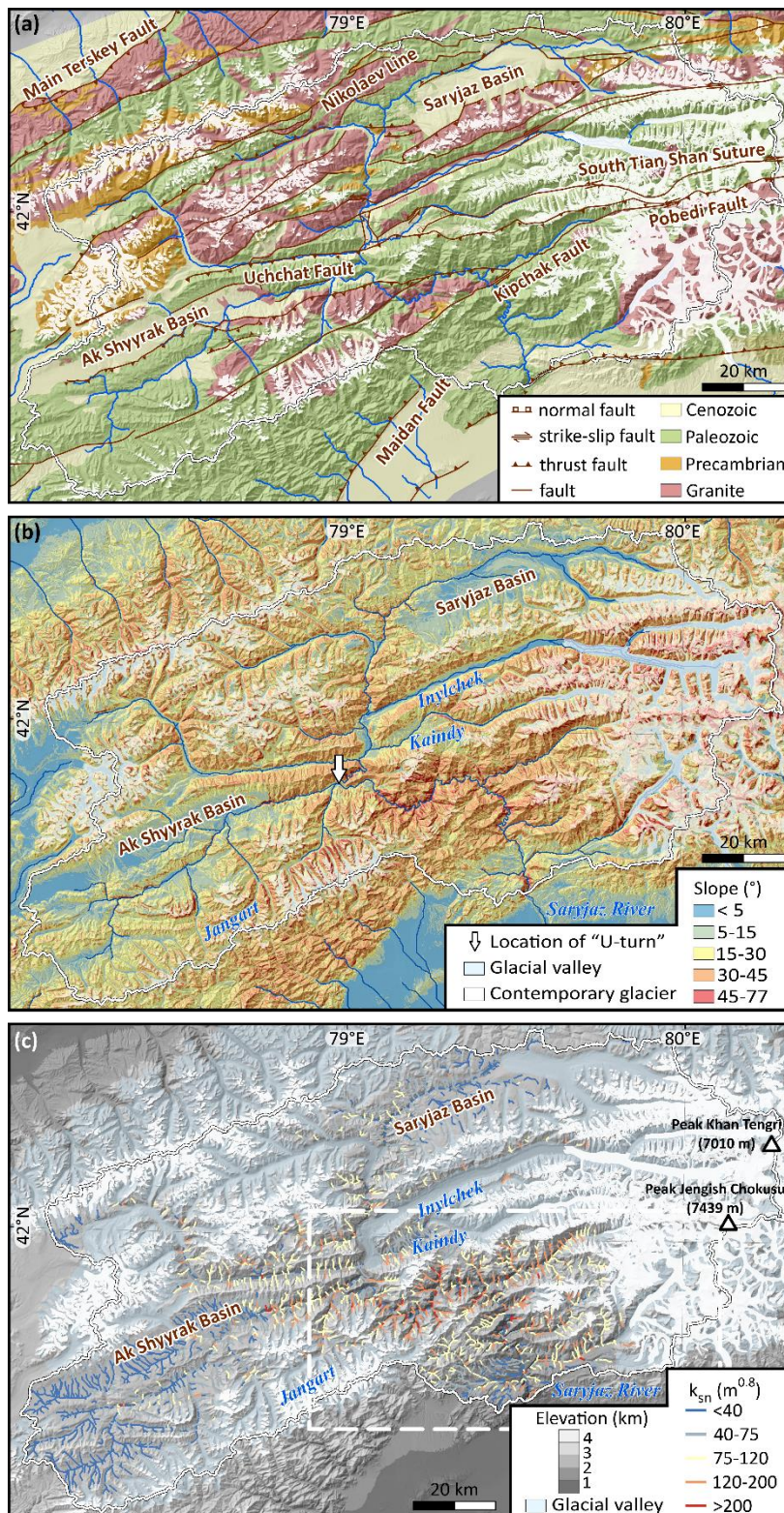
Figure 2 (a) Geological map (Mikolaichuk et al., 2008; Zhukov et al., 2008), (b) slope map, and (c) channel steepness (k_{sn}) map of the

Saryjaz catchment, overlain on shaded topographic relief. White shading in all three maps indicates contemporary glaciers. Arrow in (b) shows the location of the "U-turn" in Saryjaz trunk stream. Dashed box in (c) indicates extent of Fig. 4.

2.2 Geological setting

The Tian Shan is bounded by the Tarim Basin to the south and Kazakh platform to the north (Burbank et al., 1999). The basement of the Tian Shan is made up of three terranes, the North Tian Shan, Middle Tian Shan and South Tian Shan, separated by two Paleozoic sutures that also accumulated significant sinistral strike-slip: the Late Devonian-Early Carboniferous Nikolaev Line and the Late Carboniferous South Tian Shan Suture (Burtman, 1975, 2010; Biske, 1995; Bazhenov et al., 2003; Bazhenov and Mikolaichuk, 2004; Fig. 2a).

The ancestral Tian Shan was formed by the collision of the Tarim and Junggar blocks, and continental accretion during the Paleozoic (e.g. Dumitru et al., 2001; Xiao et al., 2013). From Mesozoic to early Cenozoic time, the Tian Shan experienced periodic reactivation in response to several distal collisions; these included collisions between the Lhasa block and Eurasia during the Late Jurassic, between the Kohistan-Ladakh arc and Eurasia in the Late Cretaceous, between Siberia and the Mongolia-North China Block during the Late Cretaceous – early Paleogene, and the most recent collision between India and Asia since the early Paleogene (Watson et al., 1987; Hendrix et al., 1992; Sobel and Dumitru, 1997; Dumitru et al., 2001; Jolivet et al., 2010; Glorie et al., 2011; Macaulay et al., 2014).

Cenozoic deformation in the South Tian Shan, based on sedimentary and thermochronology records, initiated during the late Oligocene to early Miocene (~30-22 Ma) (Sobel et al., 2006a; Glorie et al., 2011; Macaulay et al., 2014; Rolland et al., 2020). Paleozoic structures, including the Nikolaev Line and the South Tian Shan Suture, have localized the Cenozoic deformation, while the terranes in between generally behaved as rigid blocks (Jolivet et al., 2010; Glorie et al., 2011; Macaulay et al., 2013, 2014; Rolland et al., 2020). This pattern of deformation has resulted in the uplift of widely-spaced mountain ranges, separated by intermontane basins (Burbank et al., 1999; Macaulay et al., 2014). Two such basins occur in the Saryjaz river, the Saryjaz and Ak Shyyrak basins, which are mainly filled with Eocene – Pliocene conglomerate, sandstone, and siltstone as well as Recent deposits of pebbles, boulders and clay (Mikolaichuk et al., 2008; Mikolaichuk et al., 2022). Enhanced exhumation of the intervening mountain ranges is recorded during the late Miocene (~12-8 Ma) and Plio-Pleistocene (< 5 Ma; Sobel et al., 2006b; Macaulay et al., 2013, 2014; Rolland et al., 2020), possibly resulting from an interplay between climate change and tectonic deformation (Sobel et al., 2006b; Rolland et al., 2020; Chang et al., 2021).

Two faults that were demonstrably active during the Quaternary, the Maidan fault to the southwest and the South Tian Shan fault to the southeast, form the southern boundary of the central South Tian Shan (Fig. 1b). Based on dating of Quaternary sediments and analysis of geomorphological features, late-Quaternary movement along the Maidan fault has been estimated to be around 1.2 mm/yr vertically and 1.6 mm/yr laterally (Wu et al., 2019). Frequent, moderate to major earthquakes along the southwest boundary of the South Tian Shan and its frontal Jiashi-Kepingtage region (e.g., the 1902 Mw 7.7 Atushi earthquake and the 2020 Mw 6.4 Jiashi earthquake) document its current tectonic activity (Lü et al., 2021). The South Tian Shan fault, together with the structures in the Kuqa foreland basin, has developed a fold-and-thrust belt since the Oligocene

(Izquierdo-Llavall et al., 2018; Li et al., 2022). Along the South Tian Shan, N-S shortening decreases from ~17.5 to ~3 mm/yr from west to east, with deformation patterns changing from orthogonal shortening to sinistral transpression along the main structures (Yang et al., 2008). At the easternmost end of the South Tian Shan, total late-Cenozoic shortening has been estimated

145 to be only 10-15 km (Cunningham et al. 2003; Li et al. 2022). Modern average denudation rates across the eastern South Tian Shan, derived from cosmogenic nuclides, are limited to between ~0.1 and 0.2 mm/yr, lower than the estimated crustal thickening rate of around 1.3 mm/yr (Charreau et al., 2023). These patterns indicate that the topography of the Tian Shan is not in steady state, but rather is still growing laterally and vertically (Charreau et al., 2017, 2023).

2.3 Knickpoints and transient landscape evolution

150 Knickpoints (or knickzones) refer to a convex step in a river's overall concave longitudinal profile (e.g. Whipple, 2004; Whipple et al., 2013). Knickpoints can be classified as: (1) vertical-step knickpoints, corresponding to local river steepening, (2) slope-break knickpoints, with a distinct change in river gradient downstream, or (3) knickzones if they are not discrete points (Kirby and Whipple, 2012; Lague, 2014; Neely et al., 2017). All three types of knickpoints can be either stable, i.e., anchored in space, or transient and mobile, generally migrating upstream. Stable knickpoints may occur due to lithologic

155 change or structures accommodating differential rock uplift such as folds or faults (Crosby and Whipple, 2006; Wobus et al., 2006; Gallen and Wegmann, 2017; Giachetta and Willett, 2018; Marrucci et al., 2018; Fadul et al., 2022; Seagren et al., 2022). Transient knickpoints show no direct relationship with geological features and originate due to a change in basin dynamics. In a longitudinal profile, transient knickpoints commonly separate an upstream, unadjusted stream segment from an adjusted, steepened downstream portion characterized by faster incision rates (Wobus et al., 2006; Kirby and Whipple, 2012; Lague,

160 2014; Gallen and Wegmann, 2017; Schwanghart and Scherler, 2020). Two common drivers for transient knickpoint generation and retreat include: (1) drainage capture or diversion (Fig. 3a, 3c) and (2) base-level drop (Fig. 3b, 3d). Each process leads to specific topographic characteristics of knickpoints that can be used to infer the driver for knickpoint generation, as well as its timing, if an independent calibration of knickpoint retreat rate can be made.

River capture can divert a stream into a neighbouring stream, leaving anomalies like sharp (i.e., ≥ 90°) bends, abandoned river

165 valleys, wind-gaps, and knickpoints near the point of the capture (Bishop, 1995; Seagren and Schoenbohm, 2019; Fadul et al., 2022). Water discharge will increase in the capturing stream, triggering incision (Bishop, 1995; Giachetta and Willett, 2018; Rohrmann et al., 2023). Incision of the main stem of the capturing steam will in turn trigger a transient wave of incision that proceeds up tributary valleys. In this scenario, knickpoints that occur along tributaries are initiated nearly simultaneously, moving upstream with a constant vertical velocity (Giachetta and Willett, 2018; Niemann et al., 2001; Rohrmann et al., 2023).

170 Knickpoints generally will not occur at the same elevation, since they start their vertical migration from different elevations along the trunk stream (Fig. 3c). However, the amount of incision recorded below the knickpoint will be similar for all tributaries (Fig. 3e), and, when correcting for tributary catchment size and erodibility, all tributary knickpoints will have retreated a similar distance from the tributary junctions because they were all initiated around the same time (Fig. 3e).

Alternatively, base-level fall at the outlet of a catchment can trigger transient knickpoints throughout the catchment. As the
175 knickpoint in the trunk stream migrates upstream, it will initiate transient knickpoints in each subsequent tributary it
encounters. Those knickpoints also generally migrate up tributaries vertically at a constant rate (Niemann et al., 2001), but
with different response times depending on the distance to the outlet. Specifically, tributaries closer to the outlet (starting at
lower elevation) start migrating earlier than the ones farther upstream (Wobus et al., 2006; Gallen and Wegmann, 2017;
Schwanghart and Scherler, 2020). In this scenario, all transient knickpoints in the catchment should occur at a similar elevation
180 (Fig. 3d), but the incision depth and the onset time of incision (reflected in the distance that individual knickpoints migrated
upstream from the tributary junctions) will decrease with distance from the outlet (Fig. 3f).
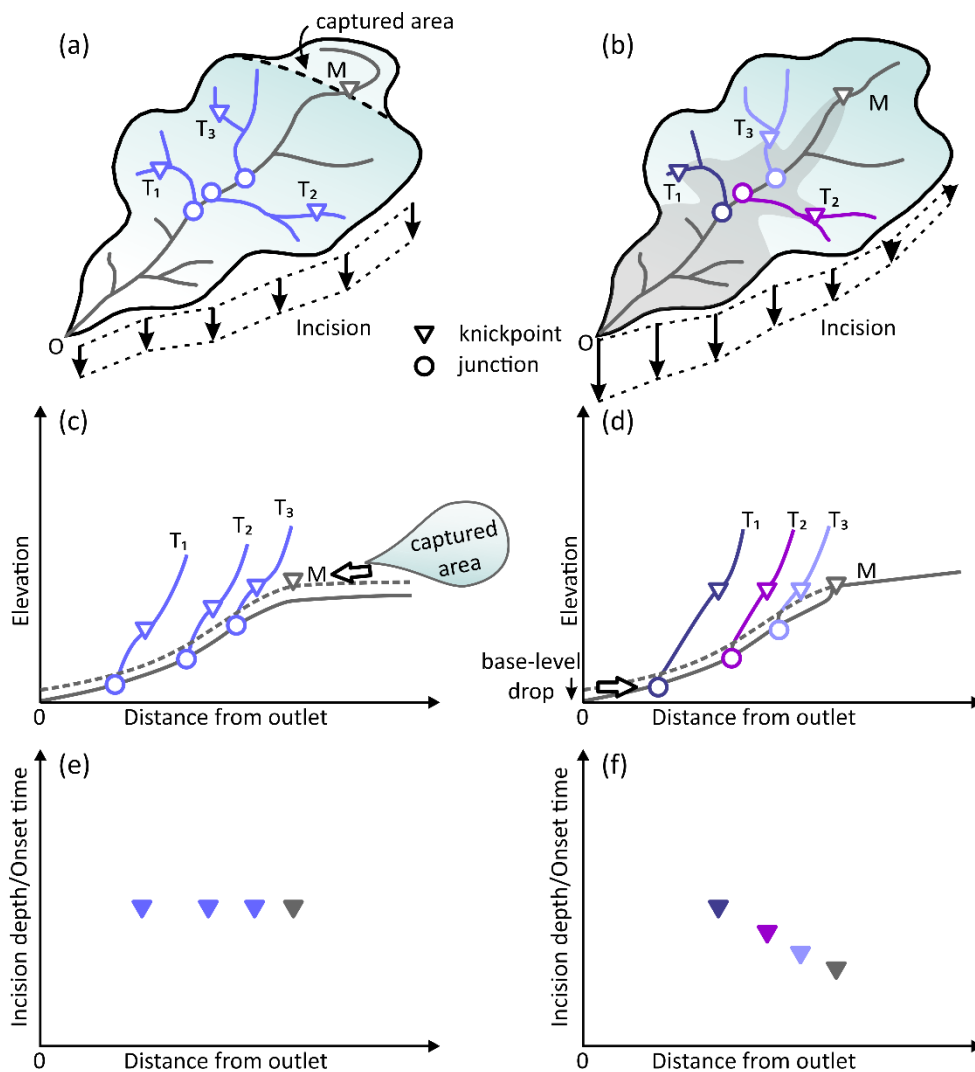
Figure 3 Sketch of two common drivers for knickpoint retreat: (a) capture and (b) base-level drop, and the resulting longitudinal profiles (c, d), incision depths and onset times of incision (e, f) as a function of distance from the outlet. M represents the main stream; T_1, T_2, and T_3 are three tributaries. Note that in (b, d and e), from T_1 to T_3, the colours of tributaries, their junctions and
185 **knickpoints change from dark to light to indicate the sequence of onset times of incision.**

3 Methodology

3.1 Topographic analysis

We used the Copernicus GLO-30 Digital Elevation Model (COP30) to analyse the topography of the central South Tian Shan.
DEM processing tools in ArcGIS, the Topographic Analysis Kit (Forte and Whipple, 2019) and Topotoolbox (Schwanghart
190 and Kuhn, 2010; Schwanghart and Scherler, 2014) were used to extract catchments, topographic metrics, and fluvial metrics.
For geological information, we used the digital geological and natural hazard maps of the Khan Tengri massif (Kyrgyzstan),
with a scale of 1:200,000 created under the ISTC Project KR-920 (Mikolaichuk et al., 2008; 2022), and the geological map of
the Kyrgyz Republic with a scale of 1:500,000 (Zhukov et al., 2008).

3.2 River-profile analysis

195 **3.2.1 Detachment-limited Stream Power Law**

The detachment-limited stream power law (Whipple and Tucker, 1999; Lague, 2014) has been widely used to describe the
topographic evolution of a landscape affected by tectonic uplift U and fluvial incision E:

$$\frac{dz}{dt} = U - E = U - KA^mS^n \tag{1}$$

Where z is landscape elevation, t is time, K is an erodibility coefficient, describing how erosion is impacted by climate,
200 lithology, hydraulic parameters, and bedload (Whipple and Tucker, 1999; Smith et al., 2022), A is upstream drainage area,
slope $S = \frac{dz}{dx}$ where x is horizontal upstream distance, and m and n are exponents.

Equation (1) can be rewritten as a power-law relation between slope (S) and drainage area (A):

$$S = k_sA^{-\theta} \tag{2}$$

where:

205

$$k_s = \left(\frac{U}{K}\right)^{1/n} \tag{3}$$

k_s, the steepness index, is useful for comparing the relative gradients of channels with different drainage areas (Flint, 1974;
Whipple and Tucker, 1999; Wobus et al., 2006), whereas the concavity index (θ) corresponds to the ratio m/n and quantifies
how rapidly the river gradient decreases downstream (Flint, 1974; Lague, 2014; Gailleton et al., 2021; Smith et al., 2022).

To compare streams among multiple catchments, a reference concavity index (θ_{ref}) is commonly used to derive a normalized
210 steepness index, k_{sn} (Whipple and Tucker, 1999; Wobus et al., 2006; Gallen and Wegmann, 2017). Typical values for θ_{ref}
range between 0.4 and 0.6, based on topographic observations and modelling studies (Kirby and Whipple, 2012; Gailleton et
al., 2021). We calculated θ_{ref} with Bayesian Optimization by minimizing a cross-validation loss (Schwanghart and Scherler,
2017) for the Saryjaz catchment. Results show a best-fit value of ∼0.4 (Fig. S1), which we consequently used for the whole
catchment.

3.2.2 χ transform

To isolate possible information on transient incision from noise in DEM data, we used χ analysis (Perron and Royden, 2013): integrating Equation (2) with distance upstream from a base-level elevation $z(x_b)$ gives:

$$z = z(x_b) + \left(\frac{U}{KA_0{}^m}\right)^{1/n} \chi \qquad (4)$$

Where A_0 is a reference drainage area and χ is an integral quantity with a dimension of distance:

$$\chi = \int_{x_b}^{x} \left(\frac{A_0}{A(x)}\right)^{m/n} dx \qquad (5)$$

In steady state, with constant U and K, Equation (4) represents a linear relationship between χ and z, and the gradient $\left(\frac{U}{KA_0{}^m}\right)^{1/n}$ is equal to k_{sn} when $A_0 = 1$. We chose 1500 m as the outlet elevation for the Saryjaz catchment.

3.3 Knickpoint analysis

3.3.1 Knickpoint identification and classification

Based on the noise-magnetic test (Schwanghart and Scherler, 2017), we chose 90 m as the tolerance to extract knickpoints using Topotoolbox. We verified the extracted knickpoints with satellite imagery to avoid potential erroneously identified knickpoints (e.g. from noise in the DEM), and classified knickpoints by describing their possible origins as (1) glacial, (2) lithologic, (3) structural (potentially linked to active faults) or (4) transient, due to either drainage reorganization, base-level drop or a change in tectonic uplift rate (e.g. Marrucci et al., 2018).

In the Saryjaz catchment, glacially impacted valleys are prominently U-shaped (Fig. S2a). Most valleys were glaciated down to an elevation of around 3000 to 3500 m, except the Inylchek valley, where glacial impacts reach below 2500 m (Stroeven et al., 2013). Tributaries to the main glaciated reaches commonly form hanging valleys, including along the Inylchek, Kaindy, and Jangart valleys (Fig. 2b-c). In a longitudinal profile, a glacial knickpoint typically appears as an abrupt, concave-up break close to a tributary confluence with a glaciated valley, either upstream in the tributary or downstream in the main valley (MacGregor et al., 2000; Valla et al., 2010; Fig. S2b). We identified glacial knickpoints as occurring within the mapped glacially impacted valleys (Stroeven et al., 2013) at elevations above 3000 to 3500 m (Fig. S3).

To identify structural and lithologic knickpoints, we referred to geologic mapping (Mikolaichuk et al., 2008) to classify faults as Cenozoic (i.e., Neotectonic, Quaternary, and active) or Paleozoic. Considering that the lithologic composition in the central South Tian Shan is rather constant for each geologic era, we classified the lithologies into four groups: (1) intrusive rock; (2) Precambrian metamorphic basement (gneiss, schist, amphibolite and marble); (3) Paleozoic sedimentary rock, with a mix of clastic (e.g. sandstone, siltstone, shale) and carbonate (e.g. limestone, dolomite) lithologies; and (4) Cenozoic clastic sediments. Knickpoints related to lithologic contrasts or to differential rock uplift are usually located on the boundaries of lithologies with different erodibilities or on mapped faults, respectively (Marrucci et al., 2018; Fadul et al., 2022). We identified lithologic and

structural knickpoints as those lying within 250 m horizontal distance from the boundaries of lithologic contacts or Cenozoic

245 faults, respectively. We verified our classification using satellite imagery (Fig. S3).

χ analysis has been widely used for recognizing transient knickpoints (e.g., Mudd et al., 2018; Smith et al., 2022). After taking

out all glacial and stable (lithological and structural) knickpoints, we used χ – z plots to identify transient reaches and slope-

break transient knickpoints, which show a sustained increase of channel steepness downstream (cf. Fig. 4). Streams used for

longitudinal profile and χ analysis were extracted with a minimum drainage area of 10^6 m^2.
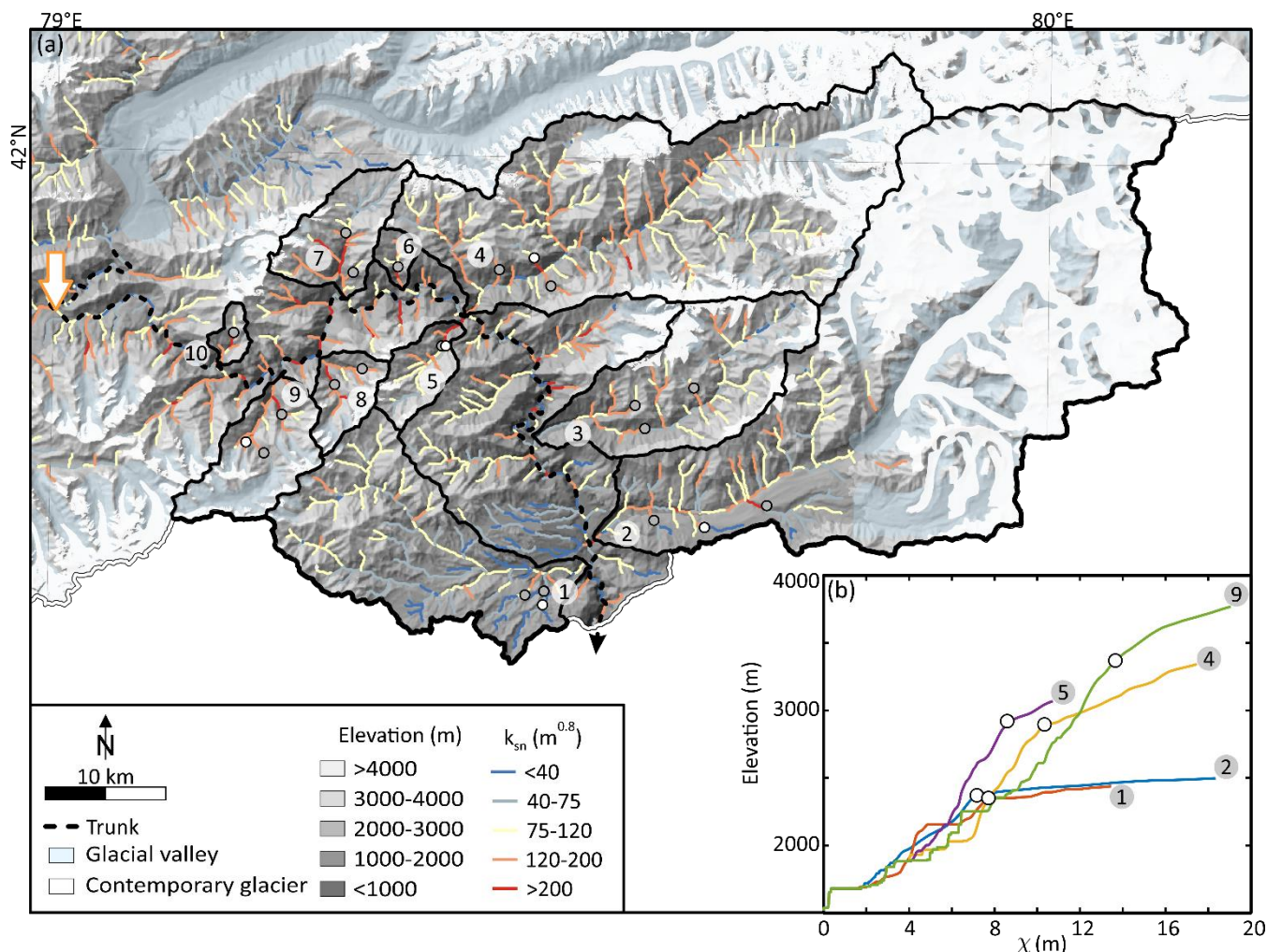
250 **Figure 4 (a) Ten sub-catchments downstream of the "U-turn" (shown as white arrow with orange outline) with transient knickpoints**
(shown as white and light grey dots with black outline); (b) representative χ – z plot of transient slope-break knickpoints. Labels
indicate the number of sub-catchments. The exact locations of these representative knickpoints are marked as white dots in (a).

3.3.2 Transient knickpoint metrics

Based on the stream-power law (Equations 1-3), the gradient (S) of a stream will respond to a change in either rock-uplift rate

255 (or base-level fall rate) or drainage area. Following an increase in base-level fall rate or rock-uplift rate, the reach closest to

the outlet reacts first, and a wave of rapid incision migrates upstream as a transient knickpoint, until completely reshaping the river to a new steady-state form, at a higher incision rate and higher gradient than before (Kirby and Whipple, 2012). By projecting the "relict" portion of the profile (i.e., upstream of the knickpoint) to the position of the outlet, one can recreate the former "steady-state" profile, and provide a minimum constraint on the magnitude of incision and/or surface uplift (Harkins

260 et al., 2007; Kirby and Whipple, 2012; Smith et al., 2022; Clementucci et al., 2023). We hereafter refer to this measurement as the "incision depth".

K is a combination of factors of erodibility, erosivity and river geometry (Smith et al., 2022). An estimation of K based on the stream-power law can be found from Equation (3) and equating $U = E$:

$$K = \frac{E}{k_{sn}{}^n} \tag{6}$$

265 If one assumes $n = 1$, the ratio of denudation rate and catchment-average channel steepness yields the erodibility coefficient value for that catchment (e.g. Kirby and Whipple, 2012; Racano et al., 2023). A value of $n = 1$, indicating a linear relationship between erosion rates/channel incision rates and channel steepness, is generally expected in regions where erosion rates are relatively low, i.e., not exceeding ca. 0.2 mm/yr (e.g. Ouimet et al., 2009; DiBiase et al., 2010).

We utilized eight ^{10}Be-derived catchment-average denudation rates (Kudriavtseva et al., in review) to calibrate an average

270 erodibility for the South Tian Shan. Unfortunately, no data are available for the Saryjaz catchment itself, in particular for the downstream reach that is of most interest here, as that region is practically inaccessible. The catchments we chose for the calibration are located within the Naryn catchment, ~200 km to the west of the Saryjaz catchment (Fig. 1b); they display similar late-Cenozoic tectonic and climatic histories, and similar lithologic compositions. We used the ArcGIS toolbox Basinga (Charreau et al., 2019) to calculate catchment-average denudation rates based on the concentrations of ^{10}Be in detrital quartz.

275 Basinga integrates variations in the Earth's magnetic field over time when considering average ^{10}Be production rates, as well as shielding due to ice or snow cover. To account for shielding, it considers that all shielded portions of the catchment contribute a ^{10}Be concentration of 0 when calculating a catchment-average production rate. These corrections are likely important, considering that glaciers exist in the four basins to the south (i.e., Cosmo catchments $1 - 4$), and regional glaciations between 15 and 28 ka affected the entire South Tian Shan (Blomdin et al., 2016). To test the possible effects of previous

280 glaciations and ice cover on catchment-average denudation rates, we compared erosion rates from three different models assuming: (1) shielding of the full extent of glacial valleys plus topographic shielding; (2) shielding from only contemporary glaciers, but without topographic shielding; and (3) the whole catchment without topographic shielding. Following Charreau et al. (2023), snow shielding was neglected for all three scenarios due to the lack of data on depth and seasonal change of snow cover in the Tian Shan region. We calculated catchment-average k_{sn} values only considering the areas that we assumed to be

285 unshielded by ice (i.e., for each scenario, the areas considered for calculating an average k_{sn} values change; Table 2).

The horizontal knickpoint propagation rate for a detachment-limited bedrock channel is defined as (Whipple and Tucker, 1999; Berlin and Anderson, 2007; Goren et al., 2014; Gallen and Wegmann, 2017):

$$\frac{dx}{dt} = KA^m S^{n-1} \tag{7}$$

Equation (7) can be solved for dt, and integrated to obtain the response time τ corresponding to the time it has taken a

290   perturbation (e.g. knickpoint) to travel from the river outlet ($x = 0$) to its current location (Whipple and Tucker, 1999; Goren et al., 2014):

$$\tau(x) = \int_0^x \frac{dx'}{KA(x')^m S(x')^{n-1}} \qquad (8)$$

Assuming $n = 1$:

$$\tau(x) = \frac{1}{KA_0^{m/n}} \int_{x_b}^x \left(\frac{A_0}{A(x)}\right)^{m/n} dx = \frac{\chi}{K} \qquad (9)$$

295   Gallen and Wegmann (2017) highlighted that Equations (7) and (8) do not incorporate rock uplift, which means that the knickpoint propagation rate, as well as the response time, is independent of the rock-uplift rate. If K and concavity are uniform, knickpoints from a common origin with the same χ values should also have the same response time τ.

We used $\chi-z$ plots along tributaries to explore the retreat pattern of transient, slope-break knickpoints in the Saryjaz catchment. Subsequently, we measured (1) elevation, (2) incision depth, (3) χ calculated from each tributary junction, and (4) k_{sn} of stream

300   reaches downstream and upstream of the knickpoints, and plotted these values against the upstream distance of the tributary junctions along the trunk.

4 Results

4.1 Topographic and fluvial metrics

The central South Tian Shan is characterized by high-elevation and high-relief topography, separated by relatively flat

305   intramontane basins. In the Saryjaz catchment, slopes of the high-relief areas (e.g., downstream of the "U-turn") reach up to ~ 76°, while they are less than 15° in the intramontane Ak Shyyrak and Saryjaz basins (Fig. 2b). Another noteworthy topographic feature is that, unlike the Saryjaz Basin, which has uniform low slopes, slope gradients in the Ak Shyyrak Basin increase eastward from almost flat at the divide with the Naryn River in the west to ~30–45° near the junction of the Ak Shyyrak River with the main stem of the Saryjaz River in the east (Fig. 2b).

310   The pattern of channel steepness (k_{sn}) is consistent with the topographic patterns: steeper reaches are mostly located downstream of the "U-turn", whereas the flattest reaches occur in the Ak Shyyrak and Saryjaz basins, particularly near their sources. Median k_{sn} values are 95.9 $m^{0.8}$ and 44.6 $m^{0.8}$ for areas downstream and upstream of the "U-turn", respectively (Fig. 5a). Similar to the distribution of slopes, streams from the Ak Shyyrak Basin also show increasing k_{sn} values, from < 40 $m^{0.8}$ in the west to ~ 120 $m^{0.8}$ in the east, whereas values are consistently low throughout the Saryjaz Basin (Fig. 2b). From swath

315 profiles mapped along the main stem of the Saryjaz catchment, an abrupt increase in relief downstream of the "U-turn"
separates a rugged downstream region from relatively gentle-relief upstream regions (cf. Fig. 6a).
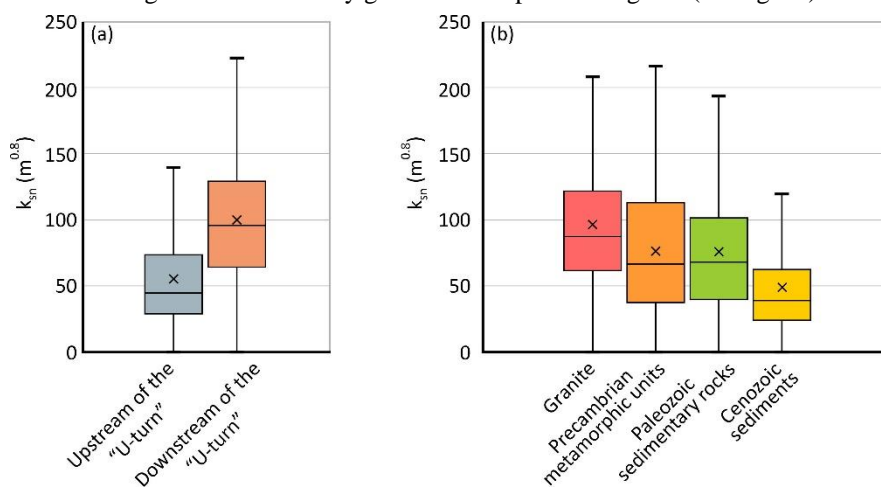
Figure 5 Box plots of k_{sn} split by (a) upstream and downstream of the "U-turn", and (b) four main lithologic units in the Saryjaz catchment.

According to the stream-power law (Equations 1-3), for a constant rock-uplift rate and concavity index, channel steepness
320 should be higher in areas of more resistant bedrock, characterized by lower erodibility (K) values (Gailleton et al., 2021; Fadul
et al., 2022). Box-plots of k_{sn} values from the Saryjaz catchment confirm this prediction: the plutonic rock unit generates the
steepest channels with a median k_{sn} of 87.0 m$^{0.8}$, whereas Precambrian metamorphic basement and Paleozoic sedimentary
rocks (including clastics and carbonates) have similar average values of 67.2 and 68.1 m$^{0.8}$, respectively. Cenozoic sediments
show a distinctively lower average k_{sn} value of 39.1 m$^{0.8}$ (Fig. 5b). Compared with the major change in k_{sn} values across the
325 "U- turn", however, k_{sn} values from bedrock units (i.e., excluding the Cenozoic sediments) are rather concordant.

4.2 Knickpoint patterns

We automatically extracted 351 knickpoints from the Saryjaz catchment. By comparing with geological maps and satellite
images, we identified 209 glacial knickpoints, 21 lithologic knickpoints, and 13 structural knickpoints. The remaining 108
knickpoints do not show any clear relationship with glacial or geological mapping (Fig. S3).
330 Using $\chi - z$ plots, 24 major slope-break knickpoints and 84 vertical-step ones were identified (Fig. S3, S4). All of the major,
transient slope-break knickpoints are located in tributaries downstream of the "U-turn". Based on their locations, we delineated
10 sub-catchments along the trunk of the Saryjaz catchment and labeled them 1 to 10, starting from near the outlet (Fig. 4a).
As shown in Table 1 and Figure 6b, most of these major transient knickpoints are located at elevations between ~ 2000 m and
~3500 m. Elevations of knickpoints generally increase with upstream distance up to 80 km from the outlet. Exceptions include
335 two knickpoints from sub-catchment 3 (i.e., 18.9 km from the outlet) that lie at elevations of more than 3000 m, and one
knickpoint from sub-catchment 10 (i.e., 74.2 km from the outlet), which has an elevation less than 2500 m; these three
knickpoints do not appear to follow the same trend as other knickpoints with similar distances from the outlet (Fig. 6b). Note

that upstream "Distance from outlet" is defined here as the distance from the main-stream junction of the tributary in which the knickpoint occurs to the outlet of the Saryjaz catchment (Fig. 6b-d).

340 Incision depths of the tributaries below the knickpoints vary between ~ 200 and ~ 800 m, with an average of 480 ± 181 m and no clear relationship with distance from the outlet of the Saryjaz catchment (Table 1, Figs. S4, 6c). To assess patterns of knickpoint retreat while correcting for different tributary catchment areas, we extracted χ distances of each knickpoint from the tributary junctions with the Saryjaz trunk stream. χ values calculated in this way lie between 3 and 8 m for most sub-catchments, with an average of 5.4 ± 1.5 m (Table 1), although three knickpoints show χ values beyond the standard deviation

345 (Fig. 6d). Note that these are the same knickpoints that plot above/below the trend of increasing knickpoint elevations with distance from the outlet (Fig. 6b, 6d). k_{sn} values downstream of the knickpoints range from 66 to 376 $m^{0.8}$, with an average of 180 ± 81 $m^{0.8}$. Upstream k_{sn} values range from 13 to 150 $m^{0.8}$, with an average of 88 ± 41 $m^{0.8}$ (Table 1, Fig. S5). These k_{sn} values, both downstream and upstream of the knickpoints, slightly increase with increasing distance from the outlet of the Saryjaz catchment. The ratios of upstream / downstream k_{sn} values show a consistent value between 1 and 3, except for one

350 knickpoint from sub-catchment 2, which shows a much higher ratio of around 10 (Table 1).

Table 1. Transient knickpoints metrics

SC No. [a]	Distance[b]	SC-KP No.[c]	Long.	Lat.	Ele.	ID[d]	χ[e]	k_{sn} downstream	k_{sn} upstream	k_{sn} ratio
			(m)	(m)	(m)	(m)	(m)	$(m^{0.8})$	$(m^{0.8})$	
		SC1-KP1	374831.9	4613549.3	2350.7	554.9	7.4	74.5	25.4	2.93
SC1	6568.6	SC1-KP2	374981.9	4614749.3	2062.4	271.7	7.0	66.3	30.8	2.15
		SC1-KP3	373331.9	4614389.3	2311.7	441.2	6.3	88.5	42.9	2.06
		SC2-KP1	384131.9	4620599.3	2667.1	387.5	4.0	124.3	46.3	2.68
SC2	8368	SC2-KP2	388331.9	4619999.3	2380	635.3	6.8	125.1	12.5	10.01
		SC2-KP3	393521.9	4621829.3	2450	691.2	5.9	239.6	73.9	3.24
		SC3-KP1	382541.9	4630199.3	3038.4	336.6	10.2	128.5	96.4	1.33
SC3	18934.6	SC3-KP2	387461.9	4631639.3	3214.7	777.8	13.3	131.7	80	1.65
		SC3-KP3	383351.9	4628249.3	2396.7	306.8	5.9	128.1	65.5	1.96
		SC4-KP1	375521.9	4640159.3	2538.5	420.2	6.1	147.1	132.4	1.11
SC4	41012.3	SC4-KP2	374141.9	4642529.3	2888.3	576	6.3	257.2	78.3	3.28
		SC4-KP3	371231.9	4641539.3	2878.8	467.6	6.2	161	78	2.06
SC5	41561.6	SC5-KP1	366701.9	4635179.3	2860.8	640.3	3.4	375.6	136.2	2.76
		SC5-KP2	366401.9	4635119.3	2667.1	456.5	2.9	375.6	115.7	3.25
SC6	52451.8	SC6-KP1	362711.9	4641659.3	2679.1	204.4	3.2	201.2	106.9	1.88
SC7	56155.6	SC7-KP1	358421.9	4644569.3	3027.8	789.3	5.4	202.8	146.7	1.38
		SC7-KP2	359021.9	4641329.3	2819.9	518.7	4.8	147.2	113	1.30
SC8	62518.6	SC8-KP1	359801.9	4633229.3	3112	538.1	6.9	130	125.7	1.03
		SC8-KP2	357461.9	4631969.3	2739.6	297.2	3.1	227.3	149.8	1.52
		SC9-KP1	353081.9	4629479.3	2805.1	432.3	3.6	200.1	138.9	1.44
SC9	67526.6	SC9-KP2	350111.9	4627109.3	3355.7	596.7	7.0	163.4	56.4	2.90
		SC9-KP3	351581.9	4626269.3	3225.5	479.3	6.6	195.4	62.3	3.14
SC10	74188.9	SC10-KP1	348911.9	4635599.3	3059.3	272.7	3.2	239.9	111.1	2.16

[a] Sub-catchment No.

b Distance from the outlet

c Sub-catchment knickpoint No.

d Incision depth

e χ values from the sub-catchments

For comparison, we also identified 5 transient knickpoints upstream of the "U-turn", and added them to the elevation-distance and incision depth-distance plots (Fig. 6). These knickpoints occur in tributaries of both the main Saryjaz trunk stream and the Ak Shyyrak River (Figs. S3 and 6). These upstream knickpoints consistently lie at higher elevations, between 3000 and 3500 m, without a clear upstream trend in elevation, while the incision depths of these knickpoints are mostly below 300 m, with an average of 222 ± 57 m (Fig. 6b-c, Table 1). In summary, there are distinct differences between knickpoints downstream and upstream of the "U-turn", including (1) the downstream knickpoints show much higher incision, and (2) the downstream knickpoints show a clear increase in elevation with distance upstream, forming a band parallel to the modern river (Fig. 6a-b). Considering their similar χ values, k_{sn} ratios, and incision depths, the knickpoints downstream of the "U-turn" likely have a common origin.
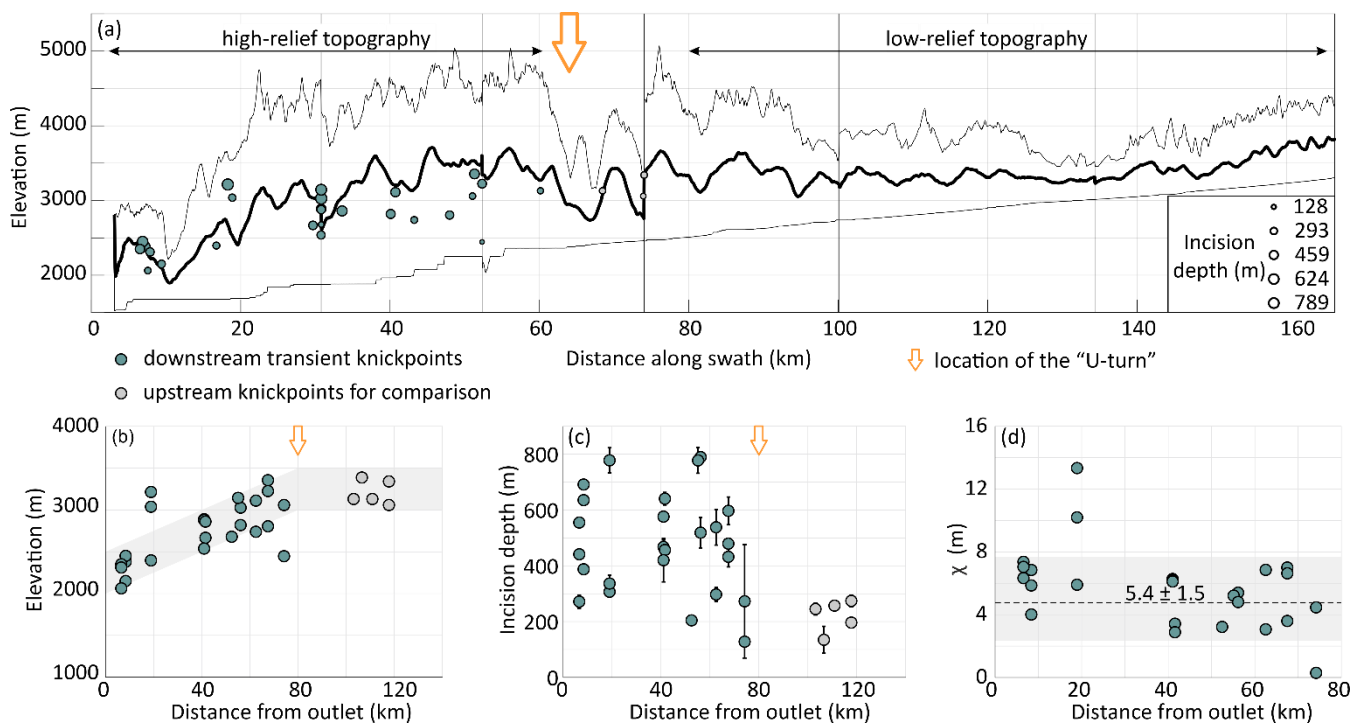
Figure 6 (a) swath profile following the main stem of the Saryjaz River, showing average (thick black line), maximum and minimum (thin black lines) elevations, as well as transient slope-break knickpoints; and plots of (b) elevation, (c) incision depth (c.f. section 3.3.2), and (d) χ-value of knickpoints (measured from the tributary junction) against distance from outlet of the tributary junction for each sub-catchment. Open orange arrow marks location of "U-turn" in the Saryjaz trunk river; "downstream" and "upstream" refer to relative location of knickpoints with respect to the "U-turn".

4.3 Timescale of transient knickpoint migration

As shown in Table 2, the catchments for which [10]Be analyses on river sands were performed (Kudriavtseva et al., in review)
370 show relatively low denudation rates between 0.038 and 0.32 mm/yr, depending on which ice-cover model was chosen. Results
for models 1 (no correction) and 2 (corrected for contemporary glacier extent) are very similar, whereas model 3 (corrected
for maximum glacier extent) leads to lower inferred denudation rates for these catchments. Integration timescales associated
with these calculated denudation rates range from 1.9 to 15.8 kyr Importantly, only the most slowly eroding catchments have
integration times that extend back to the most recent glacial advance at ca. 16 ka (Lifton et al., 2014). For that reason, including
375 a shielding calculation of the full glaciated extent of valleys is not necessarily reasonable, as the calculation assumes complete
shielding for the entire integration time. We include those calculations as an extreme end-member case, but we consider the
denudation rates derived from the other two scenarios (no shielding or shielding of contemporary glacier extents only) to be
more realistic.

Table 2. Erodibility calculation

Solution 1: Non-correction						
Basin No.	Denudation rate	Uncertainty	Mean k_{sn}	SD[a]	Drainage area	K[b]	error
	(mm/yr)	(mm/yr)	(m$^{0.8}$)		(km^2)	(m$^{0.2}$/yr)	(m$^{0.2}$/yr)
1	0.28E-01	1.80E-02	97.146	26.032	33.17	2.86E-06	9.5212E-07
2	1.76E-01	1.10E-02	90.185	28.356	36.69	1.95E-06	7.3558E-07
3	1.49E-01	9.00E-03	86.596	44.114	45.57	1.72E-06	9.8046E-07
4	2.24E-01	1.40E-02	71.623	30.205	38.07	3.13E-06	1.5144E-06
5	3.13E-01	2.00E-02	56.513	24.772	31.45	5.54E-06	2.7817E-06
6	2.55E-01	1.70E-02	41.57	10.039	24.08	6.13E-06	1.8903E-06
7	6.80E-01	4.00E-03	42.102	19.38	17.56	1.62E-06	8.3847E-07
8	3.80E-01	2.00E-03	41.164	20.134	25.80	9.23E-07	5.0011E-07
AVERAGE						2.03E-06	9.202E-07

Solution 2: Current glacier corrected						
Basin No.	Denudation rate	Uncertainty	Mean ksn	SD	Drainage area	K	error
	(mm/yr)	(mm/yr)	(m$^{0.8}$)		(km^2)	(m$^{0.2}$/yr)	(m$^{0.2}$/yr)
1	2.39E-01	1.50E-02	96.841	25.917	12.18	2.47E-06	8.1538E-07
2	1.51E-01	9.00E-03	90.259	28.732	21.85	1.67E-06	6.3226E-07
3	1.45E-01	9.00E-03	86.596	44.114	29.92	1.67E-06	9.5693E-07
4	2.24E-01	1.40E-02	71.623	30.205	17.74	3.13E-06	1.5144E-06
5	3.18E-01	2.10E-02	56.513	24.772	26.66	5.63E-06	2.8382E-06
6	2.61E-01	1.70E-02	41.57	10.039	24.08	6.28E-06	1.9252E-06
7	6.90E-02	5.00E-03	42.102	19.38	17.56	1.64E-06	8.7315E-07
8	3.90E-02	2.00E-03	41.164	20.134	25.80	9.47E-07	5.1199E-07
AVERAGE						1.92E-06	8.840E-07

Solution 3: Glacial valley corrected						
	Denudation rate	Uncertainty	Mean ksn	SD	Drainage area	K	error
	(mm/yr)	(mm/yr)	(m$^{0.8}$)		(km^2)	(m$^{0.2}$/yr)	(m$^{0.2}$/yr)

1	9.40E-02	6.00E-03	97.215	23.12	29.94	9.67E-07	2.9168E-07
2	9.40E-02	6.00E-03	91.842	25.6	32.63	1.02E-06	3.5062E-07
3	9.00E-02	5.00E-03	106.152	29.147	44.18	8.48E-07	2.7990E-07
4	9.50E-02	6.00E-03	79.375	23.84	37.72	1.20E-06	4.3506E-07
5	2.45E-01	1.60E-02	58.304	27.01	31.46	4.20E-06	2.2211E-06
6	2.55E-01	1.70E-02	41.57	10.039	24.19	6.13E-06	1.8903E-06
7	6.80E-02	4.00E-03	42.102	19.38	17.64	1.62E-06	8.3847E-07
8	3.80E-02	2.00E-03	41.164	20.134	25.91	9.23E-07	5.0011E-07
AVERAGE						1.10E-06	4.493E-07

[a] standard deviation

[b] erodibility efficiency

380

To calibrate the erodibility efficiency K, we assume $n = 1$ (Whipple et al., 2000), and use the denudation rate from ^{10}Be concentrations to represent the catchment erosion rate (e.g., Racano et al., 2023; Clementucci et al., 2023). Our derived estimates of K for the three different methods of estimating denudation rate show a consistent mean value from 1.1 to 2.0 × 10^{-6} m$^{0.2}$/yr, except for Cosmo catchments 5 and 6, which yield much higher K estimates of around 6 × 10^{-6} m$^{0.2}$/yr (Table 2,

385 Fig. 7a). These outliers can be explained by the different lithologies of the catchments: Cosmo catchments 5 and 6 equally expose Cenozoic sediments and Paleozoic sedimentary rock, whereas the other six catchments (i.e., Cosmo catchments 1, 2, 3, 4, 7 and 8) comprise predominantly Proterozoic and Paleozoic bedrock. Considering that the Saryjaz catchment, in particular the ten sub-catchments used for knickpoint retreat analysis, is characterized by relatively consistent exposure of Paleozoic intrusive and sedimentary rocks, we adopt the K values derived from Cosmo catchments 1, 2, 3, 4, 7 and 8; i.e., 1.1 ± 0.5 to

390 2.0 ± 0.9 × 10^{-6} m$^{0.2}$/yr, depending on the method of estimating denudation rates (Table 2). To test the response time to the capture event, we used the χ distance of knickpoints from each tributary junction as the retreat distances (Fig. 6d, Table S3). Following Equation 8, we find a range of response times, averaging 2.8 ± 1.3 Myr for the "no correction" denudation rates,

3.0 ± 1.4 Myr for the "current-glacier corrected" denudation rates, and 5.2 ± 2.4 Myr for "glacial-valley corrected" denudation rates (Fig. 7b).
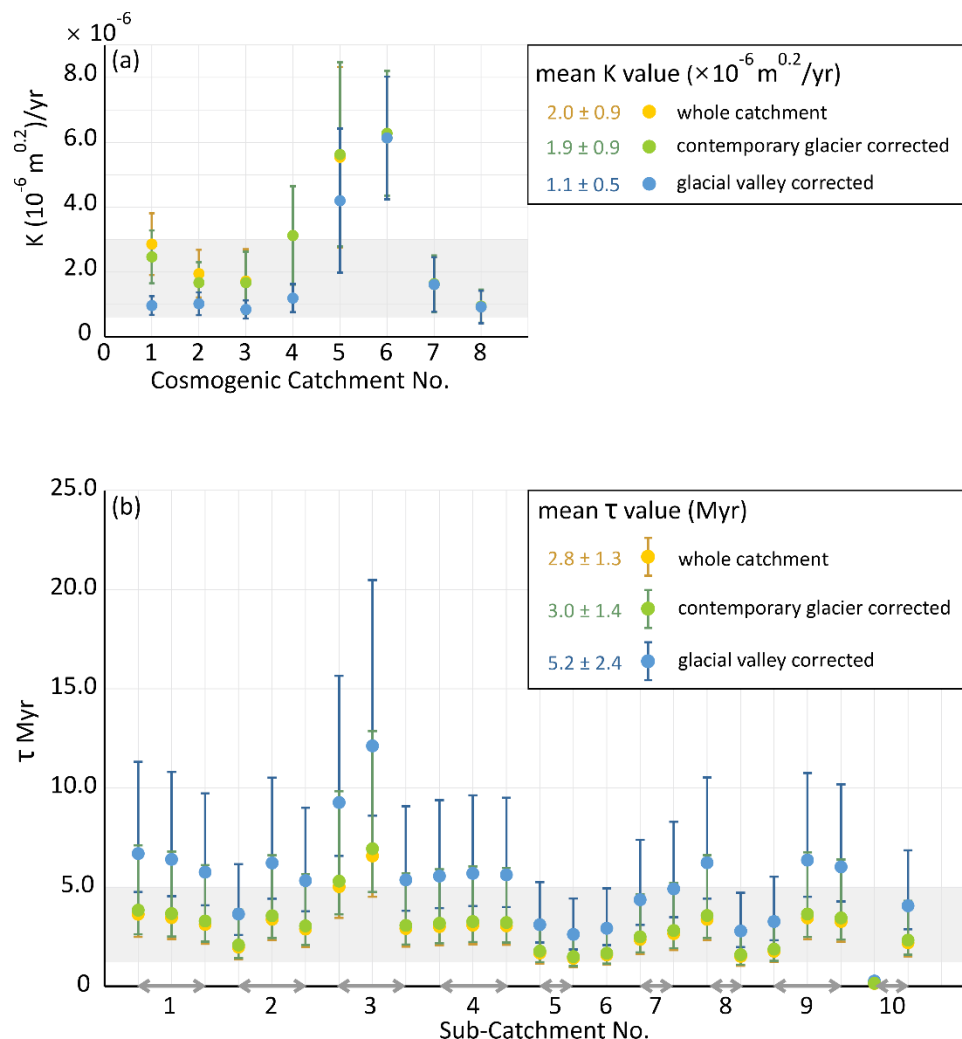
Figure 7 (a) Plots of erodibility for the eight catchments analysed with ¹⁰Be on modern sands, and (b) inferred response times for the knickpoints mapped in the ten tributary catchments downstream of the "U-turn" in the Saryjaz catchment. Both are plotted with 1σ errors. In both plots, estimates are given following the calculation of denudation rates for three scenarios: (1) "glacial-valley corrected": shielding of the full extent of glacial valleys plus topographic shielding; (2) "contemporary glacier corrected": shielding from only current glaciers; and (3) "whole catchment": without topographic or ice shielding.

5 Discussion

5.1 Origin of transient knickpoints

Although locally, we identify lithologic and structural knickpoints, their number and distribution are rather limited (Fig. S3), and they are generally not associated with substantial changes in channel steepness. Along the main stem of the Saryjaz catchment, tributary catchments downstream of the major "U-turn" show distinctly high k_{sn} values associated with steep

405   topographic slopes of up to ~76 °, and major knickpoints that appear to be transiently migrating upstream. In contrast, tributaries upstream of the "U-turn", especially within the intermontane basins, show lower slopes (mostly < 30°) and generally lack slope-break knickpoints. The knickpoints that we identify as transient occur within 40 km upstream of the "U-turn", and show relatively uniform incision depths, tributary χ values and k_{sn} ratios.

Considering theoretical predictions of the differences in patterns of knickpoint elevation and incision depth for knickpoints
410   triggered by drainage capture versus base-level fall (Fig. 3), our observations are clearly more consistent with transient knickpoint migration being triggered by drainage capture. We infer that the capture position is marked by the "U-turn" in the Saryjaz River (Figs. 2, 5). Thus, the Ak Shyyrak River corresponds to a paleo-downstream reach of the upper Saryjaz, which was captured by the lower Saryjaz River (Fig. 8). The transient knickpoints that we identified upstream of the "U-turn" (Fig. 6b-c) are distributed at elevations of around 3000 m; they show characteristics of vertical-step knickpoints (i.e., minimal
415   variation in k_{sn} downstream and upstream of the knickpoint; Lague, 2014; Neely et al., 2017) and incision depths less than 300 m. We suggest that these knickpoints are due to the same capture event that produced the knickpoints downstream: enhanced incision downstream of the "U-turn" would have triggered increased incision upstream of the capture point, as the whole river profile starts to approach a new equilibrium form (e.g., Yanites et al., 2013; Penserini et al., 2023).

5.2 Drainage evolution in the Saryjaz catchment

420   Our study provides empirical evidence for a large-magnitude capture, in which a transverse stream replaced the longitudinal lower reaches of the Saryjaz catchment near the "U-turn". We suggest that in Miocene time, a west-flowing river connected two intermontane basins, Saryjaz and Ak Shyyrak, and likely continued westward to join the current Naryn River. The southern flank of the central South Tian Shan would have represented a drainage divide between this longitudinal west-flowing drainage and short transverse systems draining into the Tarim Basin (Fig. 8a). The simplest triggering mechanism for this capture event
425   would be overtopping of the divide: during the Pliocene-Pleistocene period, the Ak Shyyrak Basin gradually filled with sediment, until river aggradation caused the west-flowing channel to eventually reach and overtop the drainage divide. An indication for this mechanism is provided by the occurrence of sedimentary remnants, inferred from satellite imagery, east of and high above the Saryjaz river in the vicinity of the "U-turn" (Fig. S6). As a result, the entire upper part of the Saryjaz Basin would have been diverted southward to flow into the Tarim Basin instead of westward through the Ak Shyyrak Basin into the
430   Naryn (Fig. 8b). The capture event would also have reversed the Ak Shyyrak river to flow east into the Saryjaz catchment rather than west into the Naryn catchment (Fig. 8b). The capture thus added substantial additional area draining to the reaches of the Saryjaz catchment downstream of the "U-turn", which would have drastically increased water discharge and increased channel incision of those downstream reaches, creating transient knickpoints that migrated from the trunk up into each tributary. The capture of the upper Saryjaz and reversal of the Ak Shyyrak River would have transformed the original NE-SW trending
435   drainage divide on the southern flank of the central South Tian Shan into the current NW-SE trending divide between the Saryjaz and Naryn catchments (Fig. 8). Today, the divide between the Saryjaz and Naryn catchments is located near Paterbashik Lake and is characterized by low slopes and low channel steepness values on both sides (Fig. S7a). However,

slightly lower χ values to the east of the divide (Fig. S7b) suggest that the divide has migrated westward along the Ak Shyyrak valley by repeated capture of upper Naryn tributaries (Bishop, 1995; Shelef and Goren, 2021) and that this process is still

440   ongoing. The elevation of the current divide between the Ak Shyyrak and the Naryn rivers at Paterbashik lake is around 3500 m, a few hundred meters higher than the highest sedimentary remnants along the Saryjaz river near the "U-turn" at around 3200 m (Fig. S6). The divide lies within Neogene sediments, providing a minimum elevation reached by the fill of the Ak Shyyrak basin prior to the capture and supporting a scenario in which capture was driven by overtopping of the Ak Shyyrak basin.

445   Recent studies indicate that drainage capture will immediately increase trunk-stream k_{sn} values for the aggressor stream downstream of the capture point due to the sudden increase in drainage area without a change in channel slope, while adjacent and tributary channel k_{sn} values remain unaffected (Giachetta and Willett, 2018; Seagren and Schoenbohm, 2019). Such a drainage reorganization and associated k_{sn} anomalies can potentially happen without a change in tectonic or climatic forcing (Seagren and Schoenbohm, 2019). Our analysis of the Saryjaz catchment demonstrates that over a long period of time after

450   the capture event, the impacts of drainage capture will migrate from the trunk to the tributaries, producing transient k_{sn} anomalies, and eventually reshaping the whole river profile into a new equilibrium state. During the transient period, the pattern of knickpoint elevations and incision depths between the tributaries and the main stem provide important diagnostic evidence of a major capture event (Giachetta and Willett, 2018; Rohrmann et al., 2023).
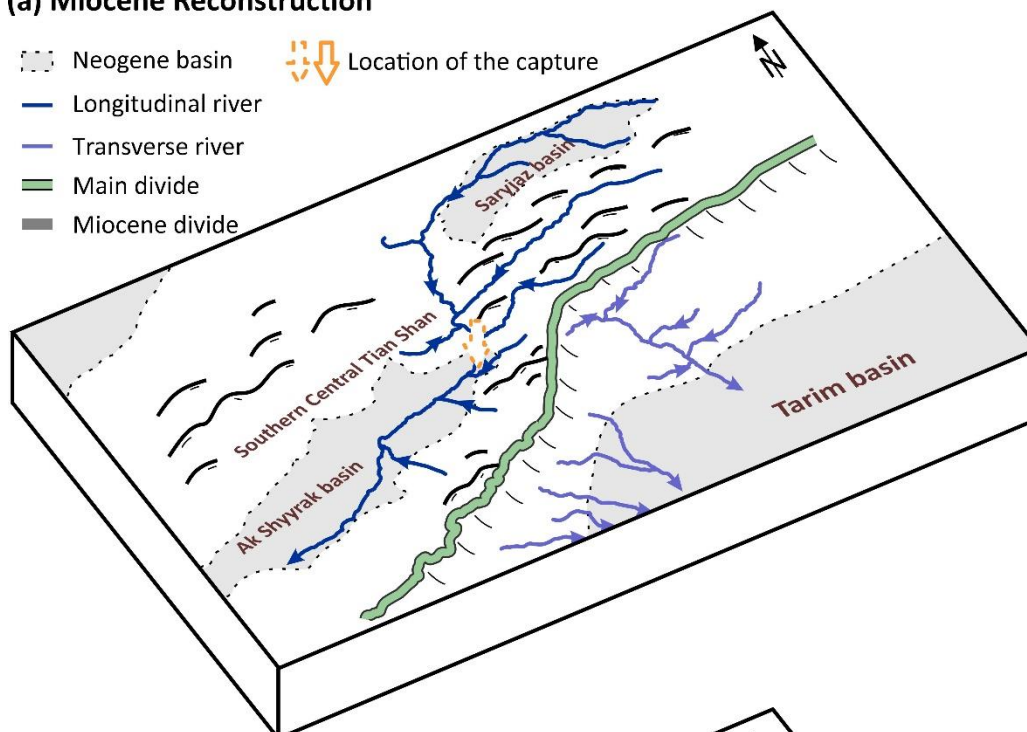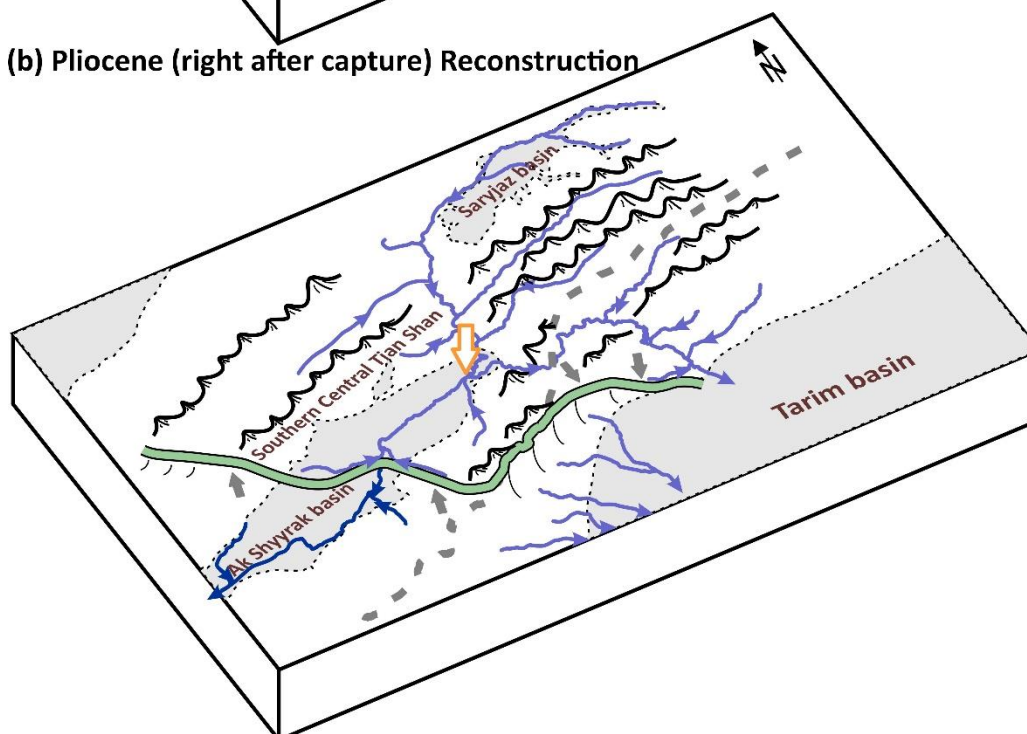
Figure 8 Topography and drainage reconstruction of the Saryjaz catchment in (a) Miocene time, before the capture, and (b) Plio-
Pleistocene time, right after the capture. Note that the main drainage divide migrated from the Miocene location (i.e. grey dash line)
to the thick green line with black edge. The direction of the migration is indicated by the grey arrows.

5.3 Possible drivers of capture

Transient knickpoint migration times calculated here indicate that the timing of the capture event likely falls between 2.8 ± 1.3 and 5.2 ± 2.4 Ma, depending on the inferred value of K (Fig. 7b). As discussed in section 4.3, the latter estimate represents an
460 extreme end-member case and we infer the most probable timing of capture to be Plio-Pleistocene (roughly between 1.5 and 4.4 Ma). Although we argue that the immediate trigger for capture was the overtopping of a pre-existing divide by the sedimentary fill of the Ak Shyyrak basin, there may be underlying tectonic or climatic drivers of this evolution. Previous studies in the regions surrounding the Ak Shyyrak Basin and the Saryjaz catchment indicate significant changes in both topography and erosion rates since the late Miocene, which may relate to the capture. We summarize events that may be
465 relevant in this context below.

Carbon $\Delta^{18}O$ values in dune and interdune deposits from the western Kepingtage range show a negative excursion between 12 and 7 Ma, indicating an arid climate, likely influenced by formation of the high-elevation barrier between the Pamir and the Tian Shan that blocked westerly moisture (Richter et al., 2022). From the Late Miocene to around 6 Ma, the South Tian Shan grew southward by uplift of the Kepingtage and Kuqa ranges. This southward growth was associated with increasing erosion
470 and sedimentation rates, as recorded by both low-temperature thermochronology and magnetostratigraphic data (Sobel et al., 2006a; Chang et al., 2019; Jia et al., 2020, 2021). Apatite (U-Th)/He cooling ages of 10 to 5 Ma have been reported from both the high-elevation Pobedi massif, south of the Pobedi fault (Fig. 1b, 2a; Rolland et al., 2020), as well as from glacial valley bottoms, for example, in the Muzart valley to the east, and the Barskoon valley to the northwest of the Saryjaz catchment (Fig. 1b; Macaulay et al., 2014; Chang et al., 2021), suggesting rapid exhumation during that time. From 9 to 4 Ma, however,
475 denudation rates in the eastern Tian Shan remained relatively steady and low, based on estimates derived from in-situ ^{10}Be in dated sedimentary records (Charreau et al., 2011; Puchol et al., 2017; Kudriavtseva et al., in review). Detrital zircon U-Pb data from the Kepingtage range indicate a sharp change in provenance from a mixed Tian Shan-Pamir source to a local source between 6 and 3.5 Ma (Rittner et al., 2016; Richter et al., 2022). This switch indicates the reactivation of uplift and deformation along the frontal Maidan fault, which contributed to the isolation and formation of the intermontane basins in the Kepingtage
480 Range and the South Tian Shan. However, our study here do not see transient knickpoints associated with this reactivation from Saryjaz catchment, which might indicate that the change in uplift rates was rather low, or that it actually occurred earlier and no longer visible as a transient signal in river profiles. Moreover, denudation rates from the southern and northern Tian Shan show an increase in variability between 3 and 1 Ma (Puchol et al., 2017), which may correspond to a transient readjustment of the landscape in response to the onset of Quaternary glacial cycles that started at around 3-2.5 Ma in the Tian
485 Shan region (Prud'homme et al., 2021).

Consequently, we consider the following possible landscape-evolution scenario. During the late Miocene, the main structures in the southern flank of the central South Tian Shan (e.g. Maidan fault, South Tian Shan fault) were reactivated as frontal thrusts, propagating southward into the foreland. The uplift of the frontal range generated sufficient relief to create a topographic barrier similar to the current Kepingtage and Kuqa ranges to the south of the Tian Shan and isolated the hinterland

490 as intermontane wedge-top basins (e.g. the Ak Shyyrak Basin), which started to fill with sediments, increasing base-level for the upstream the Saryjaz catchment (e.g. Sobel et al., 2003; Streit et al., 2017). Enhanced erosion in the high-elevation regions during the onset of Quaternary glacial cycles may have contributed to sediment production. A combination of decreased sediment transport out of the basins and increased sediment delivery rates from surrounding peaks would have accelerated basin filling, creating conditions favourable for basin overfilling and resulting drainage capture and reorganization (Streit et

495 al., 2017). In summary, we infer that both tectonic and climatic drivers may have contributed to drainage reorganization of the Saryjaz catchment, sometime between ~ 1.5 and 4.4 Ma, by influencing the filling of the intramontane Ak Shyyrak basin.

5.4 Implications for models of drainage development in mountain belts

Our observations and inferred model of drainage development in the central South Tian Shan share similarities with some of

500 the recently suggested general models for drainage development in mountain belts, but are not fully compatible with any of them. The main observations that the models should explain are: (1) drainage patterns in the South Tian Shan are longitudinal in the west, where both total shortening and shortening rates are higher, and transverse in the east, where total shortening and shortening rates are lower; and (2) the Saryjaz catchment shows evidence of transformation from a longitudinal to a transverse drainage pattern. Such a transformation is similar to what has been reported from the Atlas Mountains (Morocco), Pyrenees

505 (Spain, France) and Eastern Cordillera (Colombia; e.g. Babault et al., 2012, 2013; Struth et al., 2015). However, in the case of the central South Tian Shan, this transformation cannot be taken as an indication of a general development from longitudinal to transverse drainage as the mountain belt "matures", because both shortening rates and total shortening, as well as modern denudation rates, are higher in the west, characterized by longitudinal drainage, than in the east, characterized by transverse drainage (Charreau et al., 2017, 2023; Grin et al., 2018; Kudriavtseva et al., in review).

510 The situation in the central South Tian Shan is more akin to that in the central Andean broken foreland of NW Argentina, where Seagren et al. (2022) argued for an opposite chronology, with drainage developing from initial transverse to longitudinal patterns. Such a chronology appears consistent with the spatial pattern of transverse drainage in the east, where total shortening is lower and longitudinal drainage in the west, where higher amounts of shortening are recorded. However, the temporal drainage evolution we describe here implies transformation from longitudinal to transverse drainage, inconsistent with the

515 spatial patterns if we interpret these in a space-for-time substitution approach.

Wolf et al. (2022) suggested that longitudinal versus transverse drainage patterns indicate the state of an orogen; dominated by tectonics in the first case and by erosion in the latter. The observed drainage patterns of the South Tian Shan appear consistent with such a model. We note, however, that even in the east, surface uplift currently outpaces erosion (Charreau et al., 2017; 2023), suggesting that the orogen has not yet reached steady state. However, one could argue that parts of orogens

520 that are at the threshold between the two tectonic states (potentially including the Saryjaz catchment) could be particularly vulnerable to switches from one drainage pattern to the other induced by only minor variations in the state parameters.

The drainage evolution recorded by the Saryjaz catchment thus appears to be controlled by the transient defeat and re-establishment of through-going drainage due to the interaction of tectonics and climate (e.g. Sobel et al., 2003; Heidarzadeh

et al., 2017; Streit et al., 2017), rather than to conform to a generally applicable model of drainage development in mountain
525 belts. This conclusion underlines the importance of local contingent factors in driving drainage development relative to more
systemic drivers.

6 Conclusions

In this paper, we have studied the fluvial drainage pattern in the Saryjaz catchment located on the South Tian Shan. Our results
show that:

530 (1) A transient landscape exists in the Saryjaz catchment, especially downstream of the "U-turn" along the trunk stream,
         characterized by steepened reaches, transient knickpoints with increasing elevation upstream, consistent incision
         depths from tributary knickpoints to their intersection with the trunk stream, and consistent χ values of the knickpoints.
     (2) By considering the impacts of drainage capture versus tectonically driven base-level fall on river topographic metrics,
         we infer that the transient landscape in the Saryjaz catchment was mainly triggered by a large-magnitude drainage-
535   capture event, with an extensive longitudinal drainage system replaced by a transverse draining system.
     (3) By estimating bedrock erodibility based on basin-average denudation rates and channel steepness, combined with a
         knickpoint celerity model, we suggest that knickpoints retreat in the tributaries downstream of the "U-turn" likely
         started sometime between 1.5 and 4.4 Ma.
     (4) The capture event may have been triggered by sediments overtopping the outlet of Ak Shyyrak basin, resulting in
540   spillover of the upper Saryjaz into the lower Saryjaz river, and reversal of the Ak Shyyrak river.
     (5) From late Miocene to Plio-Pleistocene times, the South Tian Shan went through distinct tectonic and climatic changes,
         both of which may have helped to drive drainage reorganization. Considering our reconstructed landscape-evolution
         scenario, we infer that drainage reorganization can be triggered by local contingent factors that drive transient defeat
         and re-establishment of through-going drainage, and does not necessarily conform to a generally applicable model of
545   drainage development in mountain belts.

Acknowledgements

This study forms part of LxG's doctoral thesis at the University of Potsdam, supported by the Chinese Scholarship Council
(CSC) grant. We thank Wolfgang Schwanghart, Gerold Zeilinger and Stefanie Tofelde for discussions and comments.

Data Availability Statement

550 The Copernicus GLO-30 Digital Elevation Model (COP30) DEM data is a publicly available data set from https://opentopography.org/. Topotoolbox is available on GitHub at https://github.com/wschwanghart/topotoolbox.git. Topographic Analyis Kit (TAK) is also available on GitHub at https://github.com/amforte/Topographic-Analysis-Kit.git.

Author contributions

LxG: conceptualization, software, visualization, writing: original draft preparation, review & editing. PvdB: conceptualization,
555 methodology, software, writing: review&editing. TS: conceptualization, software, writing: review & editing. ES: conceptualization, writing, review & editing. SR: software, visualization, writing: review & editing. AM: software, review & editing.

Competing interests

The contact author has declared that none of the authors have any competing interests.

560 **References**

Abdrakhmatov, K. Y., Aldazhanov, S. A., Hager, B. H., Hamburger, M. W., Herring, T. A., Kalabaev, K. B., Makarov, V. I., Molnar, P., Panasyuk, S. V., Prilepin, M. T., Reilinger, R. E., Sadybakasov, I. S., Souter, B. J., Trapeznikov, Y. A., Tsurkov, V. Y., and Zubovich, A. V.: Relatively recent construction of the Tien Shan inferred from GPS measurements of present-day crustal deformation rates, Nature, 384, 450–453, https://doi.org/10.1038/384450a0, 1996.

565 Babault, J., Van Den Driessche, J., and Teixell, A.: Longitudinal to transverse drainage network evolution in the High Atlas (Morocco): The role of tectonics, Tectonics, 31, 1–15, https://doi.org/10.1029/2011TC003015, 2012.

Babault, J., Teixell, A., Struth, L., Van Den Driessche, J., Arboleya, M. L., and Tesón, E.: Shortening, structural relief and drainage evolution in inverted rifts: Insights from the Atlas Mountains, the eastern Cordillera of Colombia and the Pyrenees, Geol. Soc. Spec. Publ., 377, 141–158, https://doi.org/10.1144/SP377.14, 2013.

570 Bazhenov, M. L. and Mikolaichuk, A. V: Structural evolution of Central Asia to the north of Tibet: A synthesis of paleomagnetic and geological data, Geotectonics, 38, 379–393, 2004.

Bazhenov, M. L., Collins, A. Q., Degtyarev, K. E., Levashova, N. M., Mikolaichuk, A. V., Pavlov, V. E., and Van der Voo, R.: Paleozoic northward drift of the North Tien Shan (Central Asia) as revealed by Ordovician and Carboniferous paleomagnetism, Tectonophysics, 366, 113–141, https://doi.org/10.1016/S0040-1951(03)00075-1, 2003.

575 Berlin, M. M. and Anderson, R. S.: Modeling of knickpoint retreat on the Roan Plateau, western Colorado, J. Geophys. Res. Earth Surf., 112, 1–16, https://doi.org/10.1029/2006JF000553, 2007.

Bishop, P.: Drainage rearrangement by river capture, beheading and diversion, Prog. Phys. Geogr. Earth Environ., 19, 449–473, https://doi.org/10.1177/030913339501900402, 1995.

Biske, Y. S.: Late Paleozoic collision of the Tarimskiy and Kirghiz-Kazakh paleocontinents (English translation), Geotectonics, 29, 26–34, 1995.

Blomdin, R., Stroeven, A. P., Harbor, J. M., Lifton, N. A., Heyman, J., Gribenski, N., Petrakov, D. A., Caffee, M. W., Ivanov, M. N., Hättestrand, C., Rogozhina, I., and Usubaliev, R.: Evaluating the timing of former glacier expansions in the Tian Shan: A key step towards robust spatial correlations, Quat. Sci. Rev., 153, 78–96, https://doi.org/10.1016/j.quascirev.2016.07.029, 2016.

Boschman, L. M., Carraro, L., Cassemiro, F. A. S., de Vries, J., Altermatt, F., Hagen, O., Hoorn, C., and Pellissier, L.: Freshwater fish diversity in the western Amazon basin shaped by Andean uplift since the Late Cretaceous, Nat. Ecol. Evol., 2021.05.14.444133, https://doi.org/10.1038/s41559-023-02220-8, 2023.

Burbank, D. W., Mclean, J. K., Bullen, M., Abdrakhmatov, K. Y., and Miller, M. M.: Partitioning of intermontane basins by thrust-related folding , Tien Shan , Kyrgyzstan, 75–92, 1999.

Burtman, V. S.: Structural geology of the Tein Shan, USSR, 1975.

Burtman, V. S.: Tien Shan, Pamir, and Tibet: History and geodynamics of phanerozoic oceanic basins, Geotectonics, 44, 388–404, https://doi.org/10.1134/S001685211005002X, 2010.

Chang, J., Li, D., Min, K., Qiu, N., Xiao, Y., Wu, H., and Liu, N.: Cenozoic deformation of the Kalpin fold-and-thrust belt, southern Chinese Tian Shan: New insights from low-T thermochronology and sandbox modeling, Tectonophysics, 766, 416–432, https://doi.org/10.1016/j.tecto.2019.06.018, 2019.

Chang, J., Glorie, S., Qiu, N., Min, K., Xiao, Y., and Xu, W.: Late Miocene (10.0~6.0 Ma) Rapid Exhumation of the Chinese South Tianshan: Implications for the Timing of Aridification in the Tarim Basin, Geophys. Res. Lett., 48, 1–11, https://doi.org/10.1029/2020GL090623, 2021.

Charreau, J., Blard, P.-H., Puchol, N., Avouac, J.-P., Lallier-Vergès, E., Bourlès, D., Braucher, R., Gallaud, A., Finkel, R., Jolivet, M., Chen, Y., and Roy, P.: Paleo-erosion rates in Central Asia since 9Ma: A transient increase at the onset of Quaternary glaciations?, Earth Planet. Sci. Lett., 304, 85–92, https://doi.org/10.1016/j.epsl.2011.01.018, 2011.

Charreau, J., Saint-Carlier, D., Dominguez, S., Lavé, J., Blard, P. H., Avouac, J. P., Jolivet, M., Chen, Y., Wang, S. L., Brown, N. D., Malatesta, L. C., and Rhodes, E.: Denudation outpaced by crustal thickening in the eastern Tianshan, Earth Planet. Sci. Lett., 479, 179–191, https://doi.org/10.1016/j.epsl.2017.09.025, 2017.

Charreau, J., Blard, P., Zumaque, J., Martin, L. C. P., Delobel, T., and Szafran, L.: Basinga: A cell-by-cell GIS toolbox for computing basin average scaling factors, cosmogenic production rates and denudation rates, Earth Surf. Process. Landforms, 44, 2349–2365, https://doi.org/10.1002/esp.4649, 2019.

Charreau, J., Blard, P.-H., Lavé, J., Dominguez, S., and Li, W. S.: Unsteady topography in the eastern Tianshan due to imbalance between denudation and crustal thickening, Tectonophysics, 848, 229702, https://doi.org/10.1016/j.tecto.2022.229702, 2023.

Chen, Y., Li, W., Deng, H., Fang, G., and Li, Z.: Changes in Central Asia's Water Tower: Past, Present and Future, Sci. Rep., 6, 1–12, https://doi.org/10.1038/srep35458, 2016.

Clementucci, R., Ballato, P., Siame, L., Fox, M., Lanari, R., Sembroni, A., Faccenna, C., Yaaqoub, A., and Essaifi, A.: Surface Uplift and Topographic Rejuvenation of a Tectonically Inactive Range: Insights From the Anti-Atlas and the Siroua Massif 615 (Morocco), Tectonics, 42, https://doi.org/10.1029/2022TC007383, 2023.

Craw, D., Upton, P., Burridge, C. P., Wallis, G. P., and Waters, J. M.: Rapid biological speciation driven by tectonic evolution in New Zealand, Nat. Geosci., 9, 140–144, https://doi.org/10.1038/ngeo2618, 2016.

Crosby, B. T. and Whipple, K. X.: Knickpoint initiation and distribution within fluvial networks: 236 waterfalls in the Waipaoa River, North Island, New Zealand, Geomorphology, 82, 16–38, https://doi.org/10.1016/j.geomorph.2005.08.023, 2006.

620 DiBiase, R. A., Whipple, K. X., Heimsath, A. M., and Ouimet, W. B.: Landscape form and millennial erosion rates in the San Gabriel Mountains, CA, Earth Planet. Sci. Lett., 289, 134–144, https://doi.org/10.1016/j.epsl.2009.10.036, 2010.

Dumitru, T. A., Zhou, D., Chang, E. Z., Graham, S. A., Hendrix, M. S., Sobel, E. R., and Carroll, A. R.: Uplift, exhumation, and deformation in the Chinese Tian Shan, in: Paleozoic and Mesozoic Tectonic Evolution of Central and Eastern Asia: From Continental Assembly to Intracontinental Deformation, vol. 194, Geological Society of America, 71–99, 625 https://doi.org/10.1130/0-8137-1194-0.71, 2001.

Fadul, C. M., Oliveira, P., and Val, P.: Ongoing landscape transience in the eastern Amazon Craton consistent with lithologic control of base level, Earth Surf. Process. Landforms, 47, 3117–3132, https://doi.org/10.1002/esp.5447, 2022.

Flint, J. J.: Stream gradient as a function of order, magnitude, and discharge, Water Resour. Res., 10, 969–973, https://doi.org/10.1029/WR010i005p00969, 1974.

630 Forte, A. M. and Whipple, K. X.: Short communication: The Topographic Analysis Kit (TAK) for TopoToolbox, Earth Surf. Dyn., 7, 87–95, https://doi.org/10.5194/esurf-7-87-2019, 2019.

Frisch, K., Voigt, S., Verestek, V., Appel, E., Albert, R., Gerdes, A., Arndt, I., Raddatz, J., Voigt, T., Weber, Y., and Batenburg, S. J.: Long-Period Astronomical Forcing of Westerlies' Strength in Central Asia During Miocene Climate Cooling, Paleoceanogr. Paleoclimatology, 34, 1784–1806, https://doi.org/10.1029/2019PA003642, 2019.

635 Gailleton, B., Mudd, S. M., Clubb, F. J., Grieve, S. W. D., and Hurst, M. D.: Impact of Changing Concavity Indices on Channel Steepness and Divide Migration Metrics, J. Geophys. Res. Earth Surf., 126, https://doi.org/10.1029/2020JF006060, 2021.

Gallen, S. F. and Wegmann, K. W.: River profile response to normal fault growth and linkage: an example from the Hellenic forearc of south-central Crete, Greece, Earth Surf. Dyn., 5, 161–186, https://doi.org/10.5194/esurf-5-161-2017, 2017.

Garcia-Castellanos, D. and Jiménez-Munt, I.: Topographic Evolution and Climate Aridification during Continental Collision: 640 Insights from Computer Simulations, PLoS One, 10, e0132252, https://doi.org/10.1371/journal.pone.0132252, 2015.

Giachetta, E. and Willett, S. D.: Effects of River Capture and Sediment Flux on the Evolution of Plateaus: Insights From Numerical Modeling and River Profile Analysis in the Upper Blue Nile Catchment, J. Geophys. Res. Earth Surf., 123, 1187–1217, https://doi.org/10.1029/2017JF004252, 2018.

Glorie, S., De Grave, J., Buslov, M. M., Zhimulev, F. I., Stockli, D. F., Batalev, V. Y., Izmer, A., Van Den Haute, P.,

645   Vanhaecke, F., and Elburg, M. A.: Tectonic history of the Kyrgyz South Tien Shan (Atbashi-Inylchek) suture zone: The role of inherited structures during deformation-propagation, Tectonics, 30, https://doi.org/10.1029/2011TC002949, 2011.

Goren, L., Fox, M., and Willett, S. D.: Tectonics from fluvial topography using formal linear inversion: Theory and applications to the Inyo Mountains, California, J. Geophys. Res. Earth Surf., 119, 1651–1681, https://doi.org/10.1002/2014JF003079, 2014.

650   Grin, E., Schaller, M., and Ehlers, T. A.: Spatial distribution of cosmogenic 10Be derived denudation rates between the Western Tian Shan and Northern Pamir, Tajikistan, Geomorphology, 321, 1–15, https://doi.org/10.1016/j.geomorph.2018.08.007, 2018.

Guan, X., Yao, J., and Schneider, C.: Variability of the precipitation over the Tianshan Mountains, Central Asia. Part I: Linear and nonlinear trends of the annual and seasonal precipitation, Int. J. Climatol., 42, 118–138, https://doi.org/10.1002/joc.7235, 655   2022.

Gupta, S.: Himalayan drainage patterns and the origin of fluvial megafans in the Ganges foreland basin, Geology, 25, 11, https://doi.org/10.1130/0091-7613(1997)025<0011:HDPATO>2.3.CO;2, 1997.

Harkins, N., Kirby, E., Heimsath, A., Robinson, R., and Reiser, U.: Transient fluvial incision in the headwaters of the Yellow River, northeastern Tibet, China, J. Geophys. Res. Earth Surf., 112, 1–21, https://doi.org/10.1029/2006JF000570, 2007.

660   Heidarzadeh, G., Ballato, P., Hassanzadeh, J., Ghassemi, M. R., and Strecker, M. R.: Lake overspill and onset of fluvial incision in the Iranian Plateau: Insights from the Mianeh Basin, Earth Planet. Sci. Lett., 469, 135–147, https://doi.org/10.1016/j.epsl.2017.04.019, 2017.

Hendrix, M. S., Graham, S. A., Carroll, A. R., Sobel, E. R., McKnight, C. L., Schulein, B. J., and Wwang, Z.: Sedimentary record and climatic implications of recurrent deformation in the Tian Shan: Evidence from Mesozoic strata of the north Tarim, 665   south Junggar, and Turpan basins, northwest China, Geol. Soc. Am. Bull., 104, 53–79, https://doi.org/10.1130/0016-7606(1992)104<0053:SRACIO>2.3.CO;2, 1992.

Horton, B. K. and Decelles, P. G.: Modern and ancient fluvial megafans in the foreland basin system of the Central Andes, Southern Bolivia: Implications for drainage network evolution if foldthrust belts, Basin Res., 13, 43–63, https://doi.org/10.1046/j.1365-2117.2001.00137.x, 2001.

670   Hovius, N.: Regular spacing of drainage outlets from linear mountain belts, Basin Res., 8, 29–44, https://doi.org/10.1111/j.1365-2117.1996.tb00113.x, 1996.

Izquierdo-Llavall, E., Roca, E., Xie, H., Pla, O., Muñoz, J. A., Rowan, M. G., Yuan, N., and Huang, S.: Influence of Overlapping décollements, Syntectonic Sedimentation, and Structural Inheritance in the Evolution of a Contractional System: The Central Kuqa Fold-and-Thrust Belt (Tian Shan Mountains, NW China), Tectonics, 37, 2608–2632, 675   https://doi.org/10.1029/2017TC004928, 2018.

Jia, Y., Sun, J., Lü, L., Pang, J., and Wang, Y.: Late Oligocene-Miocene intra-continental mountain building of the Harke Mountains, southern Chinese Tian Shan: Evidence from detrital AFT and AHe analysis, J. Asian Earth Sci., 191, 104198, https://doi.org/10.1016/j.jseaes.2019.104198, 2020.

Jia, Y., Glotzbach, C., Lü, L., and Ehlers, T. A.: Cenozoic Tectono-Geomorphologic Evolution of the Pamir-Tian Shan

680 Convergence Zone: Evidence From Detrital Zircon U-Pb Provenance Analyses, Tectonics, 40, https://doi.org/10.1029/2020TC006345, 2021.

Jolivet, M., Dominguez, S., Charreau, J., Chen, Y., Li, Y., and Wang, Q.: Mesozoic and Cenozoic tectonic history of the central Chinese Tian Shan: Reactivated tectonic structures and active deformation, Tectonics, 29, n/a-n/a, https://doi.org/10.1029/2010TC002712, 2010.

685 Jourdon, A., Le Pourhiet, L., Petit, C., and Rolland, Y.: Impact of range-parallel sediment transport on 2D thermo-mechanical models of mountain belts: Application to the Kyrgyz Tien Shan, Terra Nov., 30, 279–288, https://doi.org/10.1111/ter.12337, 2018.

Kirby, E. and Whipple, K. X.: Expression of active tectonics in erosional landscapes, J. Struct. Geol., 44, 54–75, https://doi.org/10.1016/j.jsg.2012.07.009, 2012.

690 Lague, D.: The stream power river incision model: Evidence, theory and beyond, Earth Surf. Process. Landforms, 39, 38–61, https://doi.org/10.1002/esp.3462, 2014.

Li, W., Chen, Y., Yuan, X., Xiao, W., and Windley, B. F.: Intracontinental deformation of the Tianshan Orogen in response to India-Asia collision, Nat. Commun., 13, 1–8, https://doi.org/10.1038/s41467-022-30795-6, 2022.

Lifton, N., Beel, C., Hättestrand, C., Kassab, C., Rogozhina, I., Heermance, R., Oskin, M., Burbank, D., Blomdin, R.,

695 Gribenski, N., Caffee, M., Goehring, B. M., Heyman, J., Ivanov, M., Li, Y., Li, Y., Petrakov, D., Usubaliev, R., Codilean, A. T., Chen, Y., Harbor, J., and Stroeven, A. P.: Constraints on the late Quaternary glacial history of the Inylchek and Sary-Dzaz valleys from in situ cosmogenic 10Be and 26Al, eastern Kyrgyz Tian Shan, Quat. Sci. Rev., 101, 77–90, https://doi.org/10.1016/j.quascirev.2014.06.032, 2014.

Lü, L., Li, T., Chen, Z., Chen, J., Jobe, J. T., and Fang, L.: Active Structural Geometries and Their Correlation With Moderate

700 (M 5.5-7.0) Earthquakes in the Jiashi-Keping Region, Tian Shan Southwestern Front, Tectonics, 40, https://doi.org/10.1029/2021TC006760, 2021.

Macaulay, E. A., Sobel, E. R., Mikolaichuk, A., Landgraf, A., Kohn, B., and Stuart, F.: Thermochronologic insight into late Cenozoic deformation in the basement-cored Terskey Range, Kyrgyz Tien Shan, Tectonics, 32, 487–500, https://doi.org/10.1002/tect.20040, 2013.

705 Macaulay, E. A., Sobel, E. R., Mikolaichuk, A., Kohn, B., and Stuart, F. M.: Cenozoic deformation and exhumation history of the Central Kyrgyz Tien Shan, Tectonics, 33, 135–165, https://doi.org/10.1002/2013TC003376, 2014.

Macaulay, E. A., Sobel, E. R., Mikolaichuk, A., Wack, M., Gilder, S. A., Mulch, A., Fortuna, A. B., Hynek, S., and Apayarov, F.: The sedimentary record of the Issyk Kul basin, Kyrgyzstan: climatic and tectonic inferences, Basin Res., 28, 57–80, https://doi.org/10.1111/bre.12098, 2016.

710 MacGregor, K. R., Anderson, R. S., Anderson, S. P., and Waddington, E. D.: Numerical simulations of glacial-valley longitudinal profile evolution, Geology, 28, 1031–1034, https://doi.org/10.1130/0091-7613(2000)028<1031:NSOGVL>2.3.CO;2, 2000.

Malatesta, L. C. and Avouac, J. P.: Contrasting river incision in north and south Tian Shan piedmonts due to variable glacial imprint in mountain valleys, Geology, 46, 659–662, https://doi.org/10.1130/G40320.1, 2018.

715 Marrucci, M., Zeilinger, G., Ribolini, A., and Schwanghart, W.: Origin of knickpoints in an alpine context subject to different perturbing factors, stura valley, maritime alps (North-Western Italy), Geosci., 8, 10–13, https://doi.org/10.3390/geosciences8120443, 2018.

Mikolaichuk, A.V., Apayarov, F.Kh., Buchroithner, M.F., Chernavskaja, Z.I., Skrinnik, L.I., Ghes, M.D., Esmintsev, A.N., Charimov, T. A.: Digital Geological Map of the Khan Tengri Massif (Kyrgyzstan), ISTC Project No. KR-920, 2008.

720 Mikolaichuk, A., Apayarov, F., and Gordeev, D.: Correlation of geological complexes of the Khan-Tengri Mountain massif, 2022.

Morin, J., Jolivet, M., Barrier, L., Laborde, A., Li, H., and Dauteuil, O.: Planation surfaces of the Tian Shan Range (Central Asia): Insight on several 100 million years of topographic evolution, J. Asian Earth Sci., 177, 52–65, https://doi.org/10.1016/j.jseaes.2019.03.011, 2019.

725 Mudd, S. M., Clubb, F. J., Gailleton, B., and Hurst, M. D.: How concave are river channels?, Earth Surf. Dyn., 6, 505–523, https://doi.org/10.5194/esurf-6-505-2018, 2018.

Neely, A. B., Bookhagen, B., and Burbank, D. W.: An automated knickzone selection algorithm (KZ-Picker) to analyze transient landscapes: Calibration and validation, J. Geophys. Res. Earth Surf., 122, 1236–1261, https://doi.org/10.1002/2017JF004250, 2017.

730 Niemann, J. D., Gasparini, N. M., Tucker, G. E., and Bras, R. L.: A quantitative evaluation of Playfair's law and its use in testing long-term stream erosion models, Earth Surf. Process. Landforms, 26, 1317–1332, https://doi.org/10.1002/esp.272, 2001.

Ouimet, W. B., Whipple, K. X., and Granger, D. E.: Beyond threshold hillslopes: Channel adjustment to base-level fall in tectonically active mountain ranges, Geology, 37, 579–582, https://doi.org/10.1130/G30013A.1, 2009.

735 Penserini, B. D., Morell, K. D., Codilean, A. T., Fülöp, R., Wilcken, K. M., Yanites, B. J., Kumar, A., Fan, S., and Mearce, T.: Magnitude and timing of transient incision resulting from large-scale drainage capture, Sutlej River, Northwest Himalaya, Earth Surf. Process. Landforms, https://doi.org/10.1002/esp.5705, 2023.

Perron, J. T. and Royden, L.: An integral approach to bedrock river profile analysis, Earth Surf. Process. Landforms, 38, 570–576, https://doi.org/10.1002/esp.3302, 2013.

740 Prud'homme, C., Scardia, G., Vonhof, H., Guinoiseau, D., Nigmatova, S., Fiebig, J., Gerdes, A., Janssen, R., and Fitzsimmons, K. E.: Central Asian modulation of Northern Hemisphere moisture transfer over the Late Cenozoic, Commun. Earth Environ., 2, 1–8, https://doi.org/10.1038/s43247-021-00173-z, 2021.

Puchol, N., Charreau, J., Blard, P. H., Lavé, J., Dominguez, S., Pik, R., Saint-Carlier, D., and Team, A.: Limited impact of quaternary glaciations on denudation rates in central Asia, Bull. Geol. Soc. Am., 129, 479–499,
745 https://doi.org/10.1130/B31475.1, 2017.

Racano, S., Schildgen, T., Ballato, P., Yıldırım, C., and Wittmann, H.: Rock-uplift history of the Central Pontides from river-

profile inversions and implications for development of the North Anatolian Fault, Earth Planet. Sci. Lett., 616, 118231, https://doi.org/10.1016/j.epsl.2023.118231, 2023.

Richter, F., Pearson, J., Vilkas, M., Heermance, R. V., Garzione, C. N., Cecil, M. R., Jepson, G., Moe, A., Xu, J., Liu, L., and
750 Chen, J.: Growth of the southern Tian Shan-Pamir and its impact on central Asian climate, GSA Bull., 1–20, https://doi.org/10.1130/B36471.1, 2022.

Rittner, M., Vermeesch, P., Carter, A., Bird, A., Stevens, T., Garzanti, E., Andò, S., Vezzoli, G., Dutt, R., Xu, Z., and Lu, H.: The provenance of Taklamakan desert sand, Earth Planet. Sci. Lett., 437, 127–137, https://doi.org/10.1016/j.epsl.2015.12.036, 2016.

755 Rohrmann, A., Kirby, E., and Schwanghart, W.: Accelerated Miocene incision along the Yangtze River driven by headward drainage basin expansion, Sci. Adv., 9, eadh1636, https://doi.org/10.1126/sciadv.adh1636, 2023.

Rolland, Y., Jourdon, A., Petit, C., Bellahsen, N., Loury, C., Sobel, E. R., and Glodny, J.: Thermochronology of the highest central Asian massifs (Khan Tengri - Pobedi, SE Kyrgyztan): Evidence for Late Miocene (ca. 8 Ma) reactivation of Permian faults and insights into building the Tian Shan, J. Asian Earth Sci., 200, https://doi.org/10.1016/j.jseaes.2020.104466, 2020.

760 Schwanghart, W. and Kuhn, N. J.: TopoToolbox: A set of Matlab functions for topographic analysis, Environ. Model. Softw., 25, 770–781, https://doi.org/10.1016/j.envsoft.2009.12.002, 2010.

Schwanghart, W. and Scherler, D.: Short Communication: TopoToolbox 2 - MATLAB-based software for topographic analysis and modeling in Earth surface sciences, Earth Surf. Dyn., 2, 1–7, https://doi.org/10.5194/esurf-2-1-2014, 2014.

Schwanghart, W. and Scherler, D.: Bumps in river profiles: Uncertainty assessment and smoothing using quantile regression
765 techniques, Earth Surf. Dyn., 5, 821–839, https://doi.org/10.5194/esurf-5-821-2017, 2017.

Schwanghart, W. and Scherler, D.: Divide mobility controls knickpoint migration on the Roan Plateau (Colorado, USA), Geology, 48, 698–702, https://doi.org/10.1130/G47054.1, 2020.

Seagren, E. G. and Schoenbohm, L. M.: Base Level and Lithologic Control of Drainage Reorganization in the Sierra de las Planchadas, NW Argentina, J. Geophys. Res. Earth Surf., 124, 1516–1539, https://doi.org/10.1029/2018JF004885, 2019.

770 Seagren, E. G., McMillan, M., and Schoenbohm, L. M.: Tectonic Control on Drainage Evolution in Broken Forelands: Examples From NW Argentina, Tectonics, 41, https://doi.org/10.1029/2020TC006536, 2022.

Shelef, E. and Goren, L.: The rate and extent of wind-gap migration regulated by tributary confluences and avulsions, Earth Surf. Dyn., 9, 687–700, https://doi.org/10.5194/esurf-9-687-2021, 2021.

Smith, A. G. G., Fox, M., Schwanghart, W., and Carter, A.: Comparing methods for calculating channel steepness index,
775 Earth-Science Rev., 227, 103970, https://doi.org/10.1016/j.earscirev.2022.103970, 2022.

Sobel, E., Chen, J., and Heermance, R.: Late Oligocene–Early Miocene initiation of shortening in the Southwestern Chinese Tian Shan: Implications for Neogene shortening rate variations, Earth Planet. Sci. Lett., 247, 70–81, https://doi.org/10.1016/j.epsl.2006.03.048, 2006a.

Sobel, E. R. and Dumitru, T. A.: Thrusting and exhumation around the margins of the western Tarim basin during the India-
780 Asia collision, J. Geophys. Res. Solid Earth, 102, 5043–5063, https://doi.org/10.1029/96jb03267, 1997.

Sobel, E. R., Hilley, G. E., and Strecker, M. R.: Formation of internally drained contractional basins by aridity-limited bedrock incision, J. Geophys. Res. Solid Earth, 108, https://doi.org/10.1029/2002JB001883, 2003a.

Sobel, E. R., Hilley, G. E., and Strecker, M. R.: Formation of internally drained contractional basins by aridity-limited bedrock incision, J. Geophys. Res. Solid Earth, 108, https://doi.org/10.1029/2002jb001883, 2003b.

785 Sobel, E. R., Oskin, M., Burbank, D., and Mikolaichuk, A.: Exhumation of basement-cored uplifts: Example of the Kyrgyz Range quantified with apatite fission track thermochronolgy, Tectonics, 25, https://doi.org/10.1029/2005TC001809, 2006b.

Stokes, M. F., Kim, D., Gallen, S. F., Benavides, E., Keck, B. P., Wood, J., Goldberg, S. L., Larsen, I. J., Mollish, J. M., Simmons, J. W., Near, T. J., and Perron, J. T.: Erosion of heterogeneous rock drives diversification of Appalachian fishes, Science (80-.)., 380, 855–859, https://doi.org/10.1126/SCIENCE.ADD9791, 2023.

790 Streit, R. L., Burbank, D. W., Strecker, M. R., Alonso, R. N., Cottle, J. M., and Kylander-Clark, A. R. C.: Controls on intermontane basin filling, isolation and incision on the margin of the Puna Plateau, NW Argentina (~23°S), Basin Res., 29, 131–155, https://doi.org/10.1111/bre.12141, 2017.

Stroeven, A. P., Hättestrand, C., Heyman, J., Kleman, J., and Morén, B. M.: Glacial geomorphology of the Tian Shan, J. Maps, 9, 505–512, https://doi.org/10.1080/17445647.2013.820879, 2013.

795 Struth, L., Babault, J., and Teixell, A.: Drainage reorganization during mountain building in the river system of the Eastern Cordillera of the Colombian Andes, Geomorphology, 250, 370–383, https://doi.org/10.1016/j.geomorph.2015.09.012, 2015.

Sun, J., Liu, W., Liu, Z., Deng, T., Windley, B. F., and Fu, B.: Extreme aridification since the beginning of the Pliocene in the Tarim Basin, western China, Palaeogeogr. Palaeoclimatol. Palaeoecol., 485, 189–200, https://doi.org/10.1016/j.palaeo.2017.06.012, 2017.

800 Valla, P. G., Van Der Beek, P. A., and Lague, D.: Fluvial incision into bedrock: Insights from morphometric analysis and numerical modeling of gorges incising glacial hanging valleys (Western Alps, France), J. Geophys. Res. Earth Surf., 115, 1–25, https://doi.org/10.1029/2008JF001079, 2010.

Viaplana-Muzas, M., Babault, J., Dominguez, S., Van Den Driessche, J., and Legrand, X.: Modelling of drainage dynamics influence on sediment routing system in a fold-and-thrust belt, Basin Res., 31, 290–310, https://doi.org/10.1111/bre.12321, 805 2019.

Wang, Q., Zhang, P. Z., Freymueller, J. T., Bilham, R., Larson, K. M., Lai, X., You, X., Niu, Z., Wu, J., Li, Y., Liu, J., Yang, Z., and Chen, Q.: Present-day crustal deformation in China constrained by global positioning system measurements, Science (80-.)., 294, 574–577, https://doi.org/10.1126/science.1063647, 2001.

Watson, M. P., Hayward, A. B., Parkinson, D. N., and Zhang, Z. M.: Plate tectonic history, basin development and petroleum 810 source rock deposition onshore China, Mar. Pet. Geol., 4, 205–225, https://doi.org/10.1016/0264-8172(87)90045-6, 1987.

Whipple, K. X.: BEDROCK RIVERS AND THE GEOMORPHOLOGY OF ACTIVE OROGENS, Annu. Rev. Earth Planet. Sci., 32, 151–185, https://doi.org/10.1146/annurev.earth.32.101802.120356, 2004.

Whipple, K. X. and Tucker, G. E.: Dynamics of the stream-power river incision model: Implications for height limits of mountain ranges, landscape response timescales, and research needs, J. Geophys. Res. Solid Earth, 104, 17661–17674,

815 https://doi.org/10.1029/1999JB900120, 1999.

Whipple, K. X., DiBiase, R. A., and Crosby, B. T.: 9.28 Bedrock Rivers, in: Treatise on Geomorphology, vol. 9, Elsevier, 550–573, https://doi.org/10.1016/B978-0-12-374739-6.00254-2, 2013.

Wobus, C., Whipple, K. X., Kirby, E., Snyder, N., Johnson, J., Spyropolou, K., Crosby, B., and Sheehan, D.: Tectonics from topography: Procedures, promise, and pitfalls, in: Tectonics, Climate, and Landscape Evolution, vol. 398, Geological Society

820 of America, 55–74, https://doi.org/10.1130/2006.2398(04), 2006.

Wolf, S. G., Huismans, R. S., Braun, J., and Yuan, X.: Topography of mountain belts controlled by rheology and surface processes, Nature, 606, 516–521, https://doi.org/10.1038/s41586-022-04700-6, 2022.

Wu, C., Zheng, W., Zhang, P., Zhang, Z., Jia, Q., Yu, J., Zhang, H., Yao, Y., Liu, J., Han, G., and Chen, J.: Oblique Thrust of the Maidan Fault and Late Quaternary Tectonic Deformation in the Southwestern Tian Shan, Northwestern China, Tectonics,

825 38, 2625–2645, https://doi.org/10.1029/2018TC005248, 2019.

Yang, S., Li, J., and Wang, Q.: The deformation pattern and fault rate in the Tianshan Mountains inferred from GPS observations, Sci. China Ser. D Earth Sci., 51, 1064–1080, https://doi.org/10.1007/s11430-008-0090-8, 2008.

Yanites, B. J., Ehlers, T. A., Becker, J. K., Schnellmann, M., and Heuberger, S.: High magnitude and rapid incision from river capture: Rhine River, Switzerland, J. Geophys. Res. Earth Surf., 118, 1060–1084, https://doi.org/10.1002/jgrf.20056, 2013.

830 Zachos, J., Pagani, H., Sloan, L., Thomas, E., and Billups, K.: Trends, rhythms, and aberrations in global climate 65 Ma to present, Science (80-.)., 292, 686–693, https://doi.org/10.1126/science.1059412, 2001.

Zhukov, Y.V., Zakharov, I.L., Berezansky, AV., and Izraileva, R. M.: Geological map of Kyrgyz Republic, scale 1: 500 000. Agency of Geology and Mineral Resources of the Kyrgyz Republic, Bishkek, Kyrgyzstan, 2008.